

# **Use of 2D-Video Disdrometer to Derive Mean Density-Size and $Z_e$ -SR Relations: Four Snow Cases from the Light Precipitation Validation Experiment**

Gwo-Jong Huang and V. N. Bringi  
Colorado State University, Fort Collins, Colorado

Dmitri Moisseev  
University of Helsinki and Finnish Meteorological Institute, Helsinki, Finland

W. A. Petersen and L. Bliven  
NASA GSFC/Wallops Flight Facility, Wallops Island, VA

David Hudak  
Environment Canada, Downsview, Ontario, CA

Submitted to Atmospheric Research

Submitted: February 2014

---

*Corresponding author address:* Gwo-Jong Huang, Colorado State University, Fort Collins, Colorado, CO 80525.  
E-mail: gh222106@engr.colostate.edu

1 ABSTRACT

2 The application of the 2D-video disdrometer to measure fall speed and snow size distribution  
3 and to derive liquid equivalent snow rate, mean density-size and reflectivity-snow rate power  
4 law is described. Inversion of the methodology proposed by Böhm provides the pathway to use  
5 measured fall speed, area ratio and '3D' size measurement to estimate the mass of each  
6 particle. Four snow cases from the Light Precipitation Validation Experiment are analyzed with  
7 supporting data from other instruments such as Precipitation Occurrence Sensor System  
8 (POSS), Snow Video Imager (SVI), a network of seven snow gauges and three scanning C-  
9 band radars. The radar-based snow accumulations using the 2DVD-derived  $Z_e$ -SR relation are  
10 in good agreement with a network of seven snow gauges and outperform the accumulations  
11 derived from a climatological  $Z_e$ -SR relation used by the Finnish Meteorological Institute (FMI).  
12 The normalized bias between radar-derived and gauge accumulation is reduced from 96%  
13 when using the fixed FMI relation to 28% when using the  $Z_e$ -SR relations based on 2DVD data.  
14 The normalized standard error is also reduced significantly from 66% to 31%. For two of the  
15 days with widely different coefficients of the  $Z_e$ -SR power law, the reflectivity structure showed  
16 significant differences in spatial variability. Liquid water path estimates from radiometric data  
17 also showed significant differences between the two cases. Examination of SVI particle images  
18 at the measurement site corroborated these differences in terms of unrimed versus rimed snow  
19 particles. The findings reported herein support the application of Böhm's methodology for  
20 deriving the mean density-size and  $Z_e$ -SR power laws using data from 2D-video disdrometer.

21

22      **1. Introduction**

23      The measurement of liquid equivalent snow rate (*SR*) from radar has long been  
24      recognized as a difficult problem in quantitative precipitation estimation (QPE) but one  
25      of great importance for weather forecasting, hydrology, detection of aviation hazards  
26      and other remote sensing applications (e.g., ground validation for microwave radiometry  
27      from space). The validation of QPE by radar is difficult at best given the fact that  
28      accurate measurement of winter precipitation by gauges remains challenging due to the  
29      sheer variety and variability of physical properties which can change dramatically with,  
30      for example, relatively small changes in environmental conditions. Some of the  
31      important physical properties that one could list, for example, are (i) ‘3D’-size, (ii)  
32      terminal fall speed, (iii) particle size distribution, (iv) density (or, mass), (v) shape, (v)  
33      composition and (vi) porosity. Some of these attributes are not independent as  
34      evidenced by the large literature that exists in describing density (or, mass)-size and fall  
35      speed-size relations for different kinds of winter precipitation (e.g., Pruppacher and Klett  
36      2010; Mason 2010). The fall speed is also dependent on shape, composition and  
37      porosity. Thus, it follows that fall speed is fundamental to characterization of frozen  
38      precipitation followed by a good measure of ‘3D’-size, particle size distribution and  
39      porosity. From the radar reflectivity perspective, the ‘3D’-size and associated size  
40      distribution and the density (or, mass)-size relation is of fundamental importance. For  
41      Rayleigh scattering the reflectivity is directly related to  $E[m(D)^2]$  where  $m$  is the particle  
42      mass and  $E$  stand for expectation or integration over the size distribution (Ryzhkov et al.  
43      1998); however, the mass is not easily measured on a particle-by-particle basis. On the  
44      other hand, the liquid equivalent snow rate (*SR*) is directly related to  $E[m(D) V_f(D)]$

45 where  $V_f$  is the fall speed. It follows that empirical  $Z_e$ -SR power laws can be derived if  
46 mass- $D$  and  $V_f$ - $D$  power laws are assumed (e.g., Matrosov et al. 2009) and the size  
47 distribution is measured (e.g., Sekhon and Srivastava 1970). The simulations of  
48 Matrosov et al. (2009) suggest that the overall uncertainty of estimating SR from  
49 reflectivity measurements can be as high as a factor of 3 or so. A more direct method is  
50 to correlate  $Z_e$  from radar with SR measured by snow gauges (e.g., Fujiyoshi et al. 1990  
51 and references therein) which can lead to climatological  $Z_e$ -SR power law. The advent  
52 of optical-based surface disdrometers, however, has led to more accurate methods to  
53 characterize the physical properties of snow, leading to  $m$ - $D$ ,  $V_f$ - $D$  and area ratio- $D$   
54 relations that are consistent via hydrodynamic theory (Böhm 1989; Mitchell 1996;  
55 Heymsfield and Westbrook 2010). Combined with scattering models (size, shape,  
56 dielectric constant), it leads to more consistent  $Z_e$ -SR power laws (Huang et al. 2011).

57

58 There are a number of disdrometers (mainly optical) that are available (some  
59 commercial and others in the research category) that measure a sub-set of the physical  
60 parameters listed above (only instruments that can image the particles are considered  
61 here). Hanesch (1999) and Schönhuber et al. (2000) used the 1<sup>st</sup> generation 2D-video  
62 disdrometer (2DVD) which measures fall speed and two orthogonal images from which  
63 an apparent volume (also, size distribution based on '3D'-size) as well as an estimate of  
64 porosity (via the area ratio to be described later) can be computed. Later, Brandes et al.  
65 (2007) used the 2DVD to estimate the coefficient and exponent of a mean density- $D_0$   
66 power law (mainly for fluffy snow aggregates) by comparing 15-min liquid water  
67 accumulations with a collocated Geonor gauge ( $D_0$  is the median volume diameter of

the particle size distribution). They also examined the particle size distribution in detail by fitting with a gamma model and deriving correlations between the model parameters (e.g., shape parameter  $\mu$  and slope parameter  $\Lambda$ ). They conclude (in their Section 6, page 648) that, "...The video disdrometer is a powerful observational tool for studying the microphysical properties of winter storms". Further, Brandes et al. (2008) investigated power law relation between terminal fall speed and size and its dependence on temperature. The use of radar and 2DVD for estimating density-size and  $Z_e$ -SR power laws is described by Huang et al. (2010; 2011) whereas Zhang et al. (2011) demonstrated the importance of density-size power laws (empirically adjusted by fall speed) in comparing 2DVD-based reflectivity with ground radar. While the 2DVD is commercially available, a similar research instrument HVSD (Hydrometeor Velocity Size Detector; Barthazy et al. 2004) measures the fall speed and projected image in one plane. It has been used by Zawadzki et al. (2010) to investigate the natural variability of snow terminal velocity with size. They concluded that the exponent of the terminal velocity- $D$  power law could be fixed at 0.18, while the coefficient is variable from event-to-event. Szyrmer and Zawadzki (2010) describe a methodology to derive the average relationship between terminal fall velocity and the mass of snowflakes via elaboration of the methodology of Böhm (1989) proposed by earlier Hanesch (1999); the latter used the 1<sup>st</sup> generation tall 2DVD design. In fact, the development of the HVSD by Barthazy et al. (2004) followed Hanesch and lead to a simpler instrument with two parallel light planes but with much slower line scan frequency camera. The work described herein follows Szyrmer and Zawadzki (2010) but uses the 2<sup>nd</sup> generation low profile 2DVD

90 (Schöenhuber et al. 2008) to derive the  $Z_e$ -SR power law with validation provided by a  
91 network of seven snow gauges.

92

93 Another research instrument is the Snow Video Imager (SVI; Newman et al. 2009)  
94 which, unlike the line scan camera, uses a CCD (charge-coupled device) full frame  
95 camera (60 frames per second) and images are obtained almost simultaneously;  
96 however, it does not measure the fall speed. SVI software yields a size estimate of each  
97 particle as an equivalent diameter that corresponds to a circular equivalent-area  
98 diameter of the irregular shape (with holes filled). Some advantages of the SVI over the  
99 2DVD is that it has a large sample volume (twice that of the 2DVD), better pixel  
100 resolution (nominally 0.05 mm by 0.1 mm) and its measurements are less sensitive to  
101 wind. In this work, the SVI is mainly used to determine the particle size distribution for  
102 comparison with the 2DVD, and to examine samples of images to distinguish between  
103 unrimed and rimed snow particles. A new commercially available instrument is the Multi-  
104 Angle Snowflake Camera (MASC; Garrett et al. 2012) which gives high resolution (10-  
105 50  $\mu\text{m}$ ) photographs of snow particles from three viewing angles, along with their fall  
106 speed. One disadvantage is that the sample volume is small (about 1/10 of the 2DVD).

107

108 This article is organized as follows. In Section 2 the specific details of estimating the  
109 apparent volume and '3D'-apparent diameter, the adjusted particle size distribution and  
110 the application of Böhm's (1989) method are described. Section 3 constitutes the main  
111 bulk of the article and describes the 2DVD processing and derived products culminating

112 in  $Z_e$ -SR power laws for the four snow days, comparison of liquid equivalent snow  
113 accumulations derived from radar with a network of 7 snow gauges, and radar-based  
114 accumulation maps. A short summary and conclusions are given in Section 4.

115 **2. The basis for snow measurements using the 2D-video disdrometer**

116 *2.1 The apparent volume and diameter*

117 The 2DVD gives two views (front and side views; actually silhouettes) of the particle in  
118 two orthogonal planes as shown in the example in Fig. 1. It is obvious that the ‘true’  
119 volume of such an irregular particle cannot be calculated and thus we define here the  
120 apparent volume ( $VL_{app}$ ) assuming that the particle is an ellipsoid. The apparent volume  
121 is defined as an average of two ellipsoidal volumes:

122 
$$VL_{app} = \frac{\pi}{6} D_{app}^3 = \frac{VL_{app1} + VL_{app2}}{2} \dots\dots\dots(1)$$

123 where the apparent diameter is  $D_{app}$  and,

124 
$$VL_{app1} = \frac{\pi}{6} (H * W_1 * W_2) \dots\dots\dots(2)$$

125 where,

126 
$$H = \sqrt{H_1 * H_2} \dots\dots\dots(3a)$$

127

128 
$$W_{1,2} = \frac{4 * A_{e1,2}}{\pi * H} \dots\dots\dots(3b)$$

129 The  $A_{e1,2}$  are the shadow areas (see Fig. 1) from the two views. The second ellipsoid  
130 estimate,  $VL_{app2}$ , is defined as:

131 
$$VL_{app2} = \frac{\pi}{6} (HH * W_{max1} * W_{max2}) \dots\dots\dots(4)$$

132 where,

133

134  $HH = \sqrt{HH_1 * HH_2} \dots\dots\dots(5a)$

135  $HH_{1,2} = \frac{4*A_{e1,2}}{\pi*W_{max1,2}} \dots\dots\dots(5b)$

136 In (5b) the  $W_{max}$  equals the maximum width of the scan line or ‘slice’ (measured from left  
137 to right in Fig. 1); the subscripts 1,2 refer to maximum width as determined from each  
138 view. The method of calculating  $VL_{app}$  and  $D_{app}$  here generally follows Hanesch (1999)  
139 which is somewhat different from Schönhuber et al. (2000) which was used later by  
140 Brandes et al. (2007). Also, the apparent diameter ( $D_{app}$ ) is different from the ‘size’  
141 measured by instruments that give the particle image in only one plane such as aircraft-  
142 mounted imaging probes (which give the top view). The ‘size’ is often defined as the  
143 maximum distance between two pixels or the diameter of the smallest circle that  
144 completely circumscribes the image or the equivalent-area diameter (Hogan et al.  
145 2012). The latter also define the mean diameter as the mean of the particle dimensions  
146 in two orthogonal directions which they found to be better related to radar reflectivity.  
147 Since the true volume of snowflake is not known, the accuracy of our method of  
148 calculating  $VL_{app}$  cannot be determined. However, from the simulations of Wood et al.  
149 (2012) who used ellipsoidal shape models with canting it is can be inferred that the  
150 apparent diameter defined here gives a more ‘realistic’ measure of ‘3D’ size made  
151 possible by the availability of two orthogonal images from the 2DVD.

152

153 2.2 Snow size distribution (SSD)

154 In a certain time window (typically 60 seconds for 1-minute averaged size distributions),  
155 all ‘matched’ snow particles are sorted into  $M$  size bins according to the apparent  
156 diameter ( $D_{app}$ ) and the ‘un-adjusted’ size distribution  $N_m(D_i)$  is computed as:

157 
$$N_m(D_i) = \frac{1}{\Delta t * \Delta D} \sum_{j=1}^{N_i} \frac{1}{A_j * v_j} \quad [mm^{-1} m^{-3}] \dots\dots\dots(6)$$

158 where  $D_i$  is the center diameter of the  $i^{\text{th}}$  size bin (from 1 to  $M$ ) in mm;  $\Delta D$  is the bin  
159 width in mm;  $A_j$  is the measurement area in  $mm^2$ ;  $v_j$  is the fall speed in  $m s^{-1}$  and  $\Delta t$  is  
160 the time window in seconds. The fall speed measurement is fundamental to the 2DVD  
161 and relies on the ability to match the particle that falls in the upper light plane (and is  
162 imaged by Camera A) to the same particle that falls through the lower light plane and is  
163 imaged by Camera B (see Fig. 2). The match criteria used here are adapted from  
164 Hanesch (1999) as elaborated by Huang et al. (2010). If the match criteria are not  
165 satisfied then that particle is rejected; it follows that the concentration will tend to be  
166 under-estimated. To re-adjust the measured  $N_m(D_i)$  for this underestimate (assumed to  
167 be a constant factor  $\gamma$ ) the following procedure is used.

168

169 Assume that snow falls uniformly over the instrument. Then, the theoretical number of  
170 snowflakes falling through the virtual measuring area divided by the theoretical number  
171 of snowflakes falling in the scan area of each camera (shown in Fig. 2) should be equal  
172 to the ratio of these two areas as:

173 
$$\frac{\text{theoretical \# of snowflakes in virtual measuring area}}{\text{theoretical \# of snowflakes in scan area of single camera}} = \frac{100}{250} = 0.4 \dots\dots\dots(7)$$

174 Therefore, an adjustment factor  $\gamma$  is derived as:

$$175 \quad \gamma = \frac{0.4 * (\text{# of snowflakes actually counted in scan area of single camera})}{\text{# of matched snowflakes in virtual measuring area}} \quad \dots \dots \dots (8)$$

176 The “re-adjusted” concentration in each size channel ( $N(D_i)$ ) is defined as:

where  $\gamma$  is assumed constant ( $\gamma \geq 1$ ). In essence, the “raw” or unadjusted SSD is simply scaled by the factor  $\gamma$ . The validity of this adjustment will be evaluated by comparison with SSD from the snow video imager (Newman et al. 2009) as well as determining the  $\gamma$  independently by comparison with the SVI as described later in Section 3.1.

182 2.3 Böhm's Method

Böhm (1989) developed a general methodology for the terminal fall speed of solid hydrometeors based on the mass, the mean effective projected area ( $A_e$ ; see Fig. 3, also referred to as shadow area) presented to the flow, and the smallest circumscribed area ( $A$ ; circle or ellipse depending on the shape of the snow particle). Since the 2DVD can measure the fall speed of each snowflake as well as two orthogonal images (Fig. 1), we are able to compute the mass of each snowflake by inverting the Böhm equations. The assumption is that  $A_e$  which is the projected area in a plane normal to the flow, is approximately equal to the area from the side or front views (measured by the 2DVD) for irregular shaped particles. This assumption has been evaluated as being ‘reasonable’ by Szyrmer and Zawadzki (2010) who use the HVSD which gives the side view only. We first compute the Reynolds number ( $Re$ ) from fall speed ( $V_f$ ) and viscosity ( $\eta$ ) as:

195

$$Re = \frac{2 * \rho_a * V_f}{\eta} \left( \frac{A}{\pi} \right)^{\frac{1}{2}} \dots\dots\dots (10a)$$

196 where the characteristic dimension is the ‘area’ diameter ( $A$  being the area of the  
 197 smallest circumscribed ellipse or circle that completely encloses the particle image).  
 198 The  $\eta$  and air density ( $\rho_a$ ) are computed from temperature, air pressure and humidity.  
 199 Next, we compute the Davies number ( $X$ ) from  $Re$  as:

200

$$X = \left\{ \frac{\left[ \left( \frac{Re}{8.5} \right)^{\frac{1}{2}} + 1 \right]^2 - 1}{0.1519} \right\}^2 \dots\dots\dots (10b)$$

201 Finally the mass of the snowflake is computed as:

202

$$m = \frac{\pi * \eta^2 * X}{8 * g * \rho_a} \left( \frac{A_e}{A} \right)^{1/4} \dots\dots\dots (10c)$$

203 where  $g$  is the acceleration due to gravity. The ratio ( $A_e/A$ ) is referred to as the ‘area  
 204 ratio’ or  $A_r$  which is  $\leq 1$ . The MKS units are appropriate for the variables in (10). The  
 205 relative error in the estimate of mass due to uncertainty in the fixed relation between  $X$   
 206 and  $Re$ , and in the estimation of  $A_r$  has been evaluated by Szyrmer and Zawadzki  
 207 (2010) as between 40-50%. The propagation of error from (10a) to (10c) is complicated  
 208 and the reader is referred to the aforementioned reference for details.

209

210 The calculation of the minimum circumscribed area ( $A$ ) is based on the rectangle which  
 211 completely encloses the particle (the rectangle width is  $W_r$  and height is  $H$ ; see Fig. 1).

212 We first assume that, (i)  $A$  is the maximum ellipse that can be fitted inside the rectangle  
 213 and compute the area ratio  $A_e/A$  which should be  $\leq 1$ . If this ratio is greater than 1, we  
 214 assume that, (ii)  $A$  is the minimum circle that can contain the rectangle. The minimum  
 215 circumscribed area estimated from (i) usually tends to underestimate  $A$  whereas from  
 216 (ii) tends to overestimate  $A$ . The apparent volume ( $VL_{app}$ ) and apparent diameter ( $D_{app}$ )  
 217 were defined earlier, thus the density ( $\rho$ ) is obtained as the ratio of mass ( $m$ ) to  $VL_{app}$  for  
 218 each particle. Since our measurements are restricted to frozen ice precipitation, the  
 219 density is also restricted to  $\min[m/VL_{app} \quad 0.917]$  in cgs units. The mean density is  
 220 calculated for each size bin and a power law fit of the form  $\rho=aD_{app}^\beta$  is obtained for the  
 221 precipitation event. Here  $D_{app}$  is in  $mm$  and  $\rho$  is in  $g\text{ cm}^{-3}$ . The mass- $D_{app}$  power law then  
 222 is  $m=a(\pi/6)D_{app}^{\beta+3}$ .

223  
 224 For an area sampling measurement device such as the 2DVD, the liquid equivalent  
 225 snow rate ( $SR_m$ ) can be computed directly as:

$$226 SR_m = \frac{3600}{\Delta t} \sum_{i=1}^N \sum_{j=1}^M \frac{VL_j}{A_j}; \quad [mm\text{ hr}^{-1}] \dots \dots \dots (11),$$

227 where  $N$  is the number of size bins,  $M$  is the number of snowflakes in the  $i^{\text{th}}$  size bin in  
 228  $\Delta t$  (typically 60 seconds),  $VL_j$  is the liquid equivalent volume of  $j^{\text{th}}$  snowflake in  $mm^3$  (this  
 229 is the product  $\rho VL_{app}$  where  $\rho$  as a function of  $D_{app}$  is given by the power law fit) and  $A_j$   
 230 is the measurement area for the  $j^{\text{th}}$  snowflake in unit of  $mm^2$ . The adjusted snow rate is  
 231  $SR = \gamma * SR_m$  where the  $\gamma$ -factor was defined in Section 2.2.

232 We use the T-matrix (Waterman 1971; Barber and Yeh 1975) method to compute the  
233 radar cross-section of each particle and the equivalent reflectivity assuming:

234     • Refractive index: computed by the Maxwell-Garnet (1904) mixing formula  
235         with temperature from environmental data. The particle is assumed to be a  
236         mixture of ice inclusions within an air matrix with effective density  $\rho$  as a  
237         function of  $D_{app}$  as given by the 2DVD-derived power law fit

238     • Orientation: the zenith angle is Gaussian with zero mean and  $45^\circ$  standard  
239         deviation; the azimuthal angle is uniformly distributed in  $[0 \pi]$

240     • Particle Size Distribution: as in Section 2.2 which defines  $N(D)=\gamma^*N_m(D)$

241     • Particle shape: oblate spheroid with volume =  $VL_{app}$  and axis ratio = 0.8

242

243     **3. Experimental Data from LPVEx**

244 The Light Precipitation Validation Experiment (LPVEx) was held in the Fall of 2010 in  
245 the area surrounding Helsinki, Finland as a collaborative project between the Finnish  
246 Meteorological Institute (FMI), University of Helsinki and the NASA Ground Validation  
247 program (Petersen et al. 2011). While the experiment had multiple objectives and  
248 extensive suite of instruments, the focus herein is on snow measurements made at the  
249 Järvenpää site with the 2D-video disdrometer; this site also had the Precipitation  
250 Occurrence Sensor System (POSS; Sheppard and Joe 2008), the Snow Video Imager  
251 (SVI; Newman et al. 2009) and an OTT-PLUVIO2 gauge with Tretyakov and Alter  
252 shields (Ianza et al. 2006; Rasmussen et al. 2012). Three C-band polarimetric radars  
253 located at Kumpula, Vantaa and Kerava (Koskinen et al., 2011) provided for excellent

254 coverage over the Järvenpää site as well as over the network of six FMI snow gauges.  
255 Fig. 4 shows the location of the 3 radars, the Järvenpää site and the gauge network.  
256 Briefly, the three radars are nearly identical with 1° beams and using simultaneous H-V  
257 polarization on transmit and simultaneous reception of the H and V polarized back-  
258 scattered signal components via two receivers. The minimum detectable  $Z_e$  is about -10  
259 dBZ at range of 50 km. The reflectivity data from each radar covering matched areas of  
260 precipitation were used to construct the CDF of  $Z_e$  enabling accurate cross-calibration of  
261 the radars (Hirsikko et al, 2013). All the radars are Vaisala dual-polarization weather  
262 radars, a detailed description of Vantaa radar operations is presented by Saltikoff and  
263 Nevvonen, (2011).

264

265 Table 1 lists the four snow days where there was significant precipitation in Helsinki and  
266 surrounding areas. The snow events on these days were also favorable for 2DVD and  
267 other snow measuring instruments as the wind speeds were < 4 m s<sup>-1</sup> at the Järvenpää  
268 site. As seen in Table 1, the 30 Dec 2010 case could be sub-divided into two snow  
269 events based on the synoptic conditions. Similarly, the first event on 12 Jan 2011 (0800-  
270 1230 UTC) could be separated from the second event that covered the period 2230-  
271 2359 UTC which further continued the next day (13 Jan) until 0500. The liquid  
272 equivalent snow accumulations (SA) from the OTT-PLUVIO gauge ranged from 1.5 to  
273 4.2 mm.

274           3.1 Example of 2DVD processed data from 30 Dec 2010

275 As mentioned earlier, one of the fundamental measurements provided by the 2DVD is  
276 the fall speed, an example of which is provided in Fig. 5 from the first event on 30 Dec  
277 2010. The instrumental error in measuring terminal fall speeds is < 4% (for fall speeds  
278 <10 m s<sup>-1</sup>; Schönhuber et al. 2008). Such high accuracy is due in part to the plane  
279 distance calibration which is performed frequently and accounts for slight deviations in  
280 the plane distance depending on the location within the virtual measurement area (see  
281 Fig. 2); further the line scan frequency is quite high close to 55 kHz. Zawadzki et al.  
282 (2010) evaluated the fall speed measurement error for the HVSD which, to the best of  
283 our knowledge, does not account for plane distance deviations within the measurement  
284 area plus the line scan frequency is much lower, closer to 10 kHz. They estimated that  
285 the instrumental uncertainty for the HVSD is around 12% for fall speeds below 2 m s<sup>-1</sup>.  
286 While a similar analysis has not been done for the 2DVD, the contribution of  
287 instrumental error to the fall speed is expected to be much smaller than the natural  
288 variability which is depicted by the  $\pm 1\sigma$  bars in Fig. 5. It is also evident that the  
289 commonly used power law fit for  $V_f$  versus  $D$ , while analytically convenient, does not fit  
290 the data as well as an exponential fit of the form  $V_f = c[1 - d * \exp(-\kappa D_{app})]$ .

291

292 The snow size distribution (SSD) for the same event is shown in Fig. 6a where the  
293 distribution from 2DVD is compared with that derived from the Snow Video Imager  
294 (SVI). The  $\gamma$ -factor was estimated as 2.21 (Section 2b and eq. 8). Fig. 6b shows similar  
295 plot for 6 Jan. 2011 event. The agreement in the SSD is quite good given that the two  
296 instruments are based on distinctly different measurement principles and sample  
297 volumes.

298 As a further check on the estimation of  $\gamma$  using (8), the unadjusted SSD from the 2DVD  
299 has been forced to match the SVI in each size bin and the resulting mean  $\gamma_{SVI}$  is  
300 computed as:

301

$$\gamma_{SVI} = \frac{1}{N} \sum_{i=1}^N \frac{N_{SVI}(D_i)}{N_m(D_i)} \dots\dots\dots(12)$$

302 where  $N$  is the number of size bins,  $N_{SVI}(D_i)$  is the SVI-measured concentration for the  
303  $i^{th}$  bin, and the corresponding 2DVD-measured  $N_m(D_i)$  is obtained as in (6). For the case  
304 shown in Fig. 3.3 the  $\gamma_{SVI}$  was found to be 2.46 which is in close agreement with  $\gamma =$   
305 2.21. For the other snow events listed in Table 1 the  $\gamma$  comparisons are given in Table 4.  
306 As noted in the introduction the SVI gives a measure of the equal-area circular diameter  
307 which is not the same as  $D_{app}$  from the 2DVD. We ignore the different estimates of  $D$   
308 from the two instruments is so far as validation of the single camera-2DVD based  $\gamma$ -  
309 factor estimation is concerned. A more elaborate discussion of SVI estimation of  
310 different measures of  $D$  and related characterization of uncertainties in estimation of  $Z_e$   
311 and  $SR$  are given in Wood et al. (2013).

312

313 The area ratio ( $A_r$ ) discussed in Section 2c plays an important role in inverting Böhm's  
314 methodology to derive mass from the fall speed. Schmitt and Heymsfield (2010)  
315 comment that, "...area-dimensional and mass-dimensional relationships are rarely  
316 developed from the same dataset". Fig. 7 shows the frequency of occurrence plot (in log  
317 scale) of  $A_r$  vs.  $D_{app}$  for the same 30 Dec 2010 snow event. Also shown are the bin  
318 averaged mean and  $\pm 1\sigma$  standard deviation bars along with the power law fit

319  $A_r = 0.71 D_{app}^{-0.08}$ . The variability in  $A_r$  is quite large but in general agreement with  
320 Zwadzki et al. (2010) who used data from the HVSD but allowed  $A_r > 1$ . The mean fit in  
321 Fig. 7 is in good agreement with that given in Zwadzki et al; they obtain  $A_r=0.75D^{-0.17}$   
322 (but their ‘ $D$ ’ is the maximum dimension from the side-view image). A somewhat  
323 different power law fit was obtained by Schmitt and Heymsfield (2010), who used cloud  
324 imaging probe on aircraft penetrations of ice clouds aloft (this is not surprising since our  
325 results are at the surface in heavier snowfall). Schmitt and Heymsfield obtained an  
326 exponent of  $-0.25$  for the ARM data set (Heymsfield et al. 2004), but their coefficient  
327 was lower by a factor of 2.

328 The final result from Böhm’s methodology is the ability to derive a mean density- $D_{app}$   
329 power law and Fig. 8 shows the same for the 30 Dec 2010 event. While there is large  
330 variability in density for a given  $D_{app}$  (especially evident for small particles  $D_{app} < 1$  mm  
331 which might be related to difficulty in matching such particles from the two camera  
332 images resulting in erroneous fall speed determination); nevertheless, there is an  
333 inverse relation between density and  $D_{app}$  and the power law fit is  $\rho=0.15 D_{app}^{-0.86}$  for  
334 this event (Table 1 gives the coefficient and exponent for the other events). Plots of  $\rho$   
335 versus  $D_{app}$  from Table 1 using the coefficient ( $\alpha$ ) and exponent ( $\beta$ ) found herein for the  
336 four snow days are close to the mean climatological relation found by Brandes et al.  
337 (2007;  $\alpha=0.178$ ,  $\beta=-0.922$ ) as well as Holroyd (1971;  $\alpha=0.17$ ,  $\beta=-1$ ) and Fabry and  
338 Szyrmer (1999;  $\alpha=0.15$ ,  $\beta=-1$ ) with the caveat that ‘ $D$ ’ in each of the quoted references  
339 are not calculated in the same manner (see, also, Table 2 from Brandes et al. 2007).  
340 The exponent of the mass- $D_{app}$  power law is given by  $3+\beta$ ; from Table 1, the latter  
341 exponent varies between 2.04 to 2.21 generally within the range obtained by Schmitt

342 and Heymsfield (2010) based on fractal simulations of large aggregates (range between  
343 2.1–2.2), and close to the experimentally obtained exponent of 2.2 for the ARM dataset  
344 (Heymsfield et al. 2004).

345

346 The liquid equivalent snow rate (*SR*) for the 30 Dec 2010 is calculated as given in (11)  
347 using the mean  $\rho$ - $D_{app}$  power law fit from Table 1 for the two snow events that occurred  
348 on that day. The *SR* is adjusted by the  $\gamma$  factor. Fig. 9 shows the liquid equivalent snow  
349 accumulation from the 2DVD compared with the collocated OTT-PLUVIO2 gauge at the  
350 Järvenpää site. The maximum *SR* during the two snow periods occur at around 1230  
351 and 2200 UTC. The agreement between 2DVD and gauge is very good for this event  
352 (accumulations are based on 1-min *SR* from 2DVD). From Table 1, the accumulations  
353 between the 2DVD and gauge for the other days are also in good agreement. It is  
354 difficult to estimate the accuracy of the 2DVD-derived snow rate but assuming the  $\rho$ -  
355  $D_{app}$  is ‘exact’ and valid for the entire event, the dominant systematic error would be in  
356 the  $\gamma$ -adjustment parameter of the SSD. Otherwise, systematic error would primarily  
357 arise due to incorrect estimate of  $\alpha$  and secondarily  $\beta$ .

358           3.2 Reflectivity and  $Z_e$ -*SR* power law

359 The reflectivity ( $Z_e$ ) at C-band (frequency 5.5 GHz) is computed from 2DVD-measured  
360 1-min averaged  $N(D_{app})$  and the mean  $\rho$ - $D_{app}$  power law fit (for the entire event), based  
361 on the assumptions listed towards the end of Section 2.3. It is well established that for  
362 Rayleigh scattering and using the Maxwell-Garnet mixing formula (ice inclusions inside  
363 an air matrix) that  $Z_e$  can be expressed as:

364

$$Z_e = \left(\frac{1}{\rho_{ice}}\right)^2 \frac{|K_{ice}|^2}{|K_w|^2} \int_{D_{min}}^{D_{max}} \rho_{snow}^2 D^6 N(D) dD \dots\dots\dots(12)$$

365 where  $|K_{ice,w}|^2$  are the dielectric factors of solid ice and water. Since the mass of the  
 366 particle is  $m=\rho V L_{app}$ , it follows that  $Z_e$  can be simply computed (suppressing constants)  
 367 as the sum( $m^2$ ) over all the particles. Thus, the reflectivity is very sensitive to the  $m-D_{app}$   
 368 relation (or, equivalently the  $\rho-D_{app}$ ) as shown by a number of previous studies (e.g.,  
 369 Ryzhkov et al. 1998; Matrosov 2009). Errors can arise from uncertainty in the  $\gamma$ -factor  
 370 which scales the  $N(D)$  or uncertainty in the coefficient  $\alpha$  and less so in the exponent  $\beta$ .  
 371 Note that the T-matrix scattering code is used to compute  $Z_e$  at C-band frequency.

372 Fig. 10 shows time series comparison of  $Z_e$  from 2DVD, POSS [at Järvenpää site for (a)  
 373 30 Dec 2010 event and (b) 6 Jan. 2011] and the scanning Kumpula C-band radar  
 374 reflectivity data extracted over the same site (areal average over  $1^\circ \times 1$  km). The 2DVD  
 375 and POSS reflectivities are 1-min averaged whereas the Kumpula radar data were  
 376 available every 5 min. The 2DVD data are somewhat more ‘noisy’ as compared to  
 377 POSS due mainly to sampling error (the POSS has a very large sample volume by  
 378 several orders of magnitude relative to the 2DVD). The sampling error in the 2DVD  
 379 measure of  $Z_e$  was evaluated by Huang et al. (2011) by using two 2DVD units located  
 380 side-by-side at a site in Huntsville, AL. They estimated the sampling error for reflectivity  
 381 (in dBZ units) as 1.36 dB (time window for SSD integration was 1-min). They also  
 382 estimated the normalized sampling error for SR as 8.5%. The temporal correlation  
 383 between the three measures of  $Z_e$  is visually quite good.

385 By re-sampling the 2DVD and POSS reflectivities to the Kumpula radar samples, the  
386 scatter plot of 30 December 2010 case shown in Fig. 11 is obtained. The bias between  
387 POSS and 2DVD  $Z_e$  is 0.11 dB, the standard deviation is 2.9 dB, and the correlation  
388 coefficient is 0.92. The corresponding values between Kumpula radar and 2DVD are,  
389 respectively, 0.18 dB (slight radar overestimate), 4.68 dB and 0.8. The latter standard  
390 deviation values would be even lower if the 2DVD sampling error of 1.3 dB were  
391 accounted for.

The 2DVD processing described thus far gives the time series of  $Z_e$  and SR every minute (i.e., 1-min time integration) for each of the long duration ( $> 4$  h) events listed in Table 1. In order to realize a ‘stable’  $Z_e$ -SR relation the sequential intensity filtering technique (SIFT) described by Lee and Zawadzki (2005) is used along with weighted total least-squares to estimate the coefficient and exponent of the  $Z_e$ -SR power law. The basic time window (W) selected is 1 h; the SSDs are ordered by increasing  $Z_e$  in this window; and a moving average of  $M=5$  consecutively ordered SSDs is done to filter the DSDs. The same procedure is performed for the next hour of the event and so on until the entire snow duration is covered. From the filtered DSDs, the  $Z_e$  is re-computed using the appropriate  $\rho$ - $D_{app}$  power law. To re-compute SR, eq. (11) can no longer be used, rather it is computed as:

$$403 \quad SR = \frac{\pi}{6} \int \rho(D_{app}) D_{app}^3 V_f N(D_{app}) dD_{app} \dots\dots\dots(13)$$

404 where  $\rho = aD_{app}^\beta$  is the mean fit, and  $V_f = c - d^* \exp(-\kappa D_{app})$  is the mean fit to the  
 405 measured fall speeds (see example in Fig. 5).

406 Fig. 12 shows the scatter plot of  $Z_e$  versus  $SR$  and the power law fit for (a) the entire 30  
407 Dec 2010 case (i.e., inclusive of both events listed in Table 3) and (b) 6 Jan. 2011 case.  
408 Table 3 shows the  $Z_e$ - $SR$  power law fits for the other three snow days. For reference the  
409 FMI climatological relation is  $Z_e=100 SR^2$  (Saltikoff et al., 2010) It is fairly evident that for  
410 a given  $Z_e$ , the  $SR$  from the FMI relation will exceed that predicted from Table 3 power  
411 law fits. For completeness Table 4 shows the  $\gamma$ -adjustment values, and the parameters  
412  $[c\ d\ \kappa]$  of the  $V_f$ - $D_{app}$  fit.

413           3.3 Radar-derived snow accumulations

414 There were three C-band polarimetric radars operating during LPVEx, being located at  
415 (see Fig. 4) Kumpula (KUM), Kerava (KER) and Vantaa (VAN). The technical  
416 specifications can be found in (Hirsikko et al, 2013; Saltikoff and Nevvonen, 2011).  
417 When radar reflectivity is used along with a  $Z_e$ - $SR$  relation to generate, e.g., daily (liquid  
418 equivalent) snow accumulation maps, clutter and beam-blockage at low elevation  
419 angles can cause loss of signal (in the case of clutter, due to clutter filtering) which  
420 manifests as artifacts in the snow accumulation maps. To avoid this problem,  $Z_e$  data  
421 from the three radars have been composited, using maximum reflectivity factor from any  
422 of the three radars, to generate the snow accumulation map for 30 Dec 2010 as shown  
423 in Fig. 13. The peak accumulation is around 12 mm within the city of Helsinki. The solid  
424 black dots are the locations of six FMI snow gauges (Vaisala VRG101 with Tretyakov  
425 wind shield; Lanza et al. 2006) and the OTT-PLUVIO at Järvenpää site. The numbers  
426 adjacent to the gauge locations are the measured accumulations in mm. The radar  
427 composite, of course, depicts quite clearly the spatial variability without any artifacts due  
428 to clutter or beam blockages; moreover the radar-based accumulations are in good

429 agreement with the gauges. Fig. 14 shows the accumulation map using the  
430 climatological FMI  $Z_e$ -SR relation and it is readily apparent that, while the spatial  
431 variability is generally preserved, the magnitudes of the accumulations are  
432 overestimated relative to the gauges. In particular, the peak accumulations are now  
433 around 16 mm within the city.

434

435 To further detail the radar and gauge comparisons, hourly accumulations are compared  
436 in Fig. 15 from one gauge location (solid dot in Fig. 13 with 7.8 mm; this is the Porvoo  
437 Harabacka location). Whilst it is clear that the FMI climatological relation overestimates  
438 the hourly accumulations soon after the snow begins, the radar-based hourly  
439 accumulation agrees well with the gauge (and not just the event totals).

440

441 Fig. 16 (panel **a**) shows the scatter plot of daily gauge accumulations versus radar-  
442 based accumulations (extracted from the radar composites over the six gauge locations  
443 and the gauge at the Järvenpää site) for the 4 days using the  $Z_e$ -SR power laws from  
444 Table 3 while panel **b** shows the same except for using the fixed FMI climatological  $Z_e$ -  
445 SR relation. The significant feature is the dramatic reduction in bias resulting from using  
446 the  $Z_e$ -SR obtained from 2DVD data as listed in Table 3 as compared with the fixed FMI  
447 relation. The normalized bias and normalized standard error values are, respectively,  
448 28% and 30.8% when Table 3 is used versus 96.6% and 66.1% for the fixed FMI  
449 relation. Note that positive bias implies radar overestimates the gauge values. The  
450 slope of a straight line trend passing through the origin is 1.2 for panel **a** versus 1.85 for

451 panel **b**. It is reasonable to infer that the FMI gauges could have underestimated the  
452 snow amounts due to wind and type of shielding (i.e., collection efficiency < 1). Recall  
453 that the FMI gauges are Vaisala VRG101 with Tretyakov wind shields whose collection  
454 efficiency is not known as a function of wind speed. The collection efficiency (or,  
455 undercatch) is a complicated function of not only gauge/shield type and wind speed, but  
456 also the type of snow particle (dry vs. wet or unrimed vs. rimed) and particle size  
457 distribution (Thériault et al. 2012). Thus, there is considerable scatter of the collection  
458 efficiency for a given wind speed along with a systematic decrease with increasing wind  
459 speed. The latter can be estimated from Rasmussen et al. (2012; their Fig. 11) as mean  
460 collection efficiency dropping to 0.75 at wind speed of  $4 \text{ ms}^{-1}$ . If this is taken into  
461 account the bias between radar and FMI gauges seen in Fig. 16a would be further  
462 reduced.

463 *3.4 Spatial reflectivity structure for 30 Dec 2010 and 06 January 2011 cases*

464 So far, the reflectivity structure nor the environmental/synoptic conditions have been  
465 described for the different snow days, as the main emphasis was on the 2DVD data, its  
466 processing and product evaluation. However, it is useful to consider the reflectivity  
467 structure for the 30 Dec 2010 case (which had the most daily accumulation) and the 06  
468 Jan 2011 case which had the least (Table 2 or Fig. 16), accompanied by very different  
469 coefficients/exponents of the  $Z_e$ -SR power laws (respectively, 210/1.63 versus  
470 130/1.44).

472 On 30 Dec 2010 large scale snowfall areas from ESE (the first snowfall from 0800-1300  
473 UTC; see Fig. 10a) and from WNW (second snowfall from 1500-2400 UTC) merged  
474 above southern Finland. These snowfall areas were associated with two low pressure  
475 systems, one centered in Eastern Europe and the main one forming NW of  
476 Scandinavia. At around 1900 UTC the two precipitation systems have merged.  
477 ADMIRARI (Battaglia et al., 2010) LWP (liquid water path) observations reached a  
478 maximum of  $400 \text{ g m}^{-2}$  at 1500 UTC. During the observations ADMIRARI was located in  
479 the backyard of Vaisala which is around 10 km north from Kumpula radar, as shown in  
480 Fig. 4. This is the time when the warm moist area from NW had arrived to the Helsinki  
481 region. During the snowfall the LWP values were ranging between  $100-150 \text{ g m}^{-2}$ . It  
482 should be noted that these are the slant LWP observations with elevation angle of  $30^\circ$ .  
483 At the time of peak snowfall for the first event (1100-1200 UTC; see Fig. 10a) SVI  
484 images were viewed and it was observed that the main precipitation types were pristine  
485 dendritic type crystals with large aggregates composed of dendrites ( $\sim 8 \text{ mm}$ ) with little  
486 evidence of riming (Newman, personal communication). Fig. 17 shows sample SVI  
487 images at 1120 UTC near the time of maximum  $Z_e$  (see Fig. 10a).

488

489 On 06 Jan 2011 south westerly upper level flow from Scandinavia brought warm and  
490 moist air that resulted in a light to moderate snowfall lasting from 0100 to 0800 UTC.  
491 During this period (0500-0700 UTC) the ADMIRARI showed a large amount of  
492 supercooled water with LWP values exceeding  $500 \text{ g m}^{-2}$ . Examination of SVI images  
493 between 0600-0630 showed definite indications of rimed dendrites and columnar  
494 crystals followed by rimed to heavily rimed particles (perhaps graupel). Further in time,

495 large aggregates (~5-7 mm) appear to be rimed. Also, many smaller rimed  
496 snowflakes/crystals (Newman, personal communication). Fig. 18 shows examples of  
497 SVI images of rimed aggregates at 0620 UTC.

498

499 Fig. 19 shows the rather dramatically different reflectivity structures (at low elevation  
500 angle 0.5°) between the 30 Dec 2010 event (at 1000 UTC) and the 06 January 2011  
501 event (at 0610 UTC). The spatial variability is much more pronounced in the 06 January  
502 case (more cellular) as compared to the more conventional spatial variability occurring  
503 on 30 Dec. The cellular feature implies weak imbedded convection is likely with more  
504 prevalent particle riming as alluded to earlier. This is supported by analysis by Lim et al.  
505 (2013) who were able to associate higher spatial variability with enhanced riming of  
506 particles. The vertical structures are also different as depicted in the RHI scans in Fig.  
507 20 taken along the radial to the Järvenpää site Again, the 30 Dec event is much more  
508 uniform in the vertical as compared with the 06 Jan event, the latter showing more  
509 evidence of cellular structure in the vertical implying imbedded convection and  
510 enhanced riming.

511

512 Finally, in Fig. 21, the snow accumulation map for 06 Jan event is shown using the  
513 2DVD-derived  $Z_e$ -SR power law, which can be compared with Fig. 13. The snow  
514 accumulations for this event (see, also Table 1) are much smaller compared with 30  
515 Dec case additionally showing much more spatial variability. Note these are not daily

516 totals but restricted to the period 0000-0900 UTC since the 2DVD stopped working at  
517 0824 UTC on this day thereby missing another major snowfall event later on this day.

518       **4. Summary and Conclusions**

519 The estimation of the mean density-size and  $Z_e$ -SR power laws using 2D-video  
520 disdrometer measured fall speed, apparent diameter and snow size distribution (SSD)  
521 along with Böhm's (1989) methodology is described in some detail. A method for  
522 adjusting the concentration based on single camera data to account for loss of particles  
523 that do not satisfy the matching criteria (when 2 cameras are used) is shown to be  
524 reasonable when compared with Snow Video Imager (SVI)-based concentrations.  
525 Snow events which occurred on four days of the Light Precipitation Validation  
526 Experiment (LPVEx) were chosen based on light wind speeds ( $< 4 \text{ ms}^{-1}$ ) at the  
527 measurement site with liquid equivalent snow accumulations ranging from 1.5 mm to 4  
528 mm. While there is large variability of fall speed, area ratio and derived density which is  
529 attributed to natural variability of snow type, shape and porosity, the mean density- $D_{app}$   
530 (or, mass- $D_{app}$ ) and  $Z_e$ -SR power laws do vary from event-to-event. The reflectivity  
531 derived from the 2DVD data is shown to be in good agreement with collocated POSS  
532 and with scanning C-band radar, while the liquid equivalent snow accumulation is  
533 shown to be in good agreement with collocated OTT-PLUVIO gauge at the  
534 measurement site. The radar-based snow accumulations using the 2DVD-derived  $Z_e$ -  
535 SR relations for the four days are in good agreement with a network of six FMI snow  
536 gauges (and the OTT-PLUVIO gauge) and outperform the accumulations derived from a  
537 climatological  $Z_e$ -SR relation used by the Finnish Meteorological Institute (FMI). The  
538 normalized bias between radar-derived and gauge accumulation is reduced from 96%

539 (overestimate by the FMI climatological relation) to 28% when using the  $Z_e$ -SR based  
540 on 2DVD data. The normalized standard error is also reduced significantly from 66% to  
541 31%. While the FMI gauges were equipped with Tretyakov wind shields,  
542 undercatchment due to wind cannot be ignored and could account for underestimation  
543 of snow accumulations by 20-30% for wind speeds in the range  $3\text{-}4 \text{ ms}^{-1}$ ; this would  
544 reduce the bias between radar and gauge accumulations even further.

545

546 For two of the days with widely different coefficients of the  $Z_e$ -SR power law, the  
547 reflectivity structure showed significant differences in spatial variability (both horizontal  
548 and vertical). Liquid water path estimates from radiometric data also showed significant  
549 differences between the two cases. Examination of SVI particle images at the  
550 measurement site corroborated these differences in terms of unrimed versus rimed  
551 snow particles.

552

553 In summary, the findings reported herein support the application of Böhm's (1989)  
554 methodology for deriving the mean density-size and  $Z_e$ -SR power laws using data from  
555 2D-video disdrometer. Evaluation of radar-based snow accumulation against a network  
556 of snow gauges independently supports the latter conclusion notwithstanding the limited  
557 number of events available for analysis.

558

559 *Acknowledgements.* Two of the authors VNB and GJH acknowledge support from  
560 NASA grants NNX10AJ11G and NNX11AK32G. DM acknowledges support from  
561 Academy of Finland grant 263333. WAP and LB acknowledge support from NASA GPM  
562 Flight Project and Dr. Ramesh Kakar, Program Manager for PMM. The authors also  
563 acknowledge Dr. Andrew Newman of NCAR for assistance in visual classification of SVI  
564 snow images for two of the events. The SVI and POSS were installed by Peter  
565 Rodriguez of Environment Canada.

566

567 **References**

568

569 Barber, P. and Yeh, C., 1975: Scattering of Electromagnetic Waves by Arbitrarily  
570 Shaped Dielectric Bodies., *Appl. Optics*, **14**, pp. 2684-2872.

571

572 Barthazy, E., Göke, S., Schefold, R. and Högl, D., 2004: An optical array instrument for  
573 shape and fall velocity measurements of hydrometeors., *J. Atmos. Oceanic Technol.*,  
574 **21**, pp. 1400-1416.

575

576 Battaglia, A., Saavedra, P., Rose, T. and Simmer, C., 2010: Characterization of  
577 Precipitating Clouds by Ground-Based Measurements with the Triple-Frequency  
578 Polarized Microwave Radiometer ADMIRARI., *J. Appl. Meteor. Climatol.*, **49**, pp. 394–  
579 414.

580

581 Böhm, H.P., 1989: A general equation for the terminal fall speed of solid hydrometeors.,  
582 *J. Atmos. Sci.*, **46**, pp. 2419-2427.

583

584 Brandes, E. A., Ikeda, K., Zhang, G., Schönhuber, M. and Rasmussen, R. M., 2007: A  
585 statistical and physical description of hydrometeor distributions in Colorado snowstorms  
586 using a video disdrometer., *J. Appl. Meteor. Climatol.*, **46**, pp. 634-650.

587

588 Brandes, E. A., Ikeda, K. and Thompson, G., 2008: Aggregate terminal  
589 velocity/temperature relations, *J. Appl. Meteor. Climatol.*, **47**, pp. 2729–2736.

590

591 Fabry, F., and Szyrmer, W., 1999: Modeling of the melting layer. Part II:  
592 *Electromagnetic. J. Atmos. Sci.*, **56**, pp. 3593–3600.

593

594 Fujiyoshi, Y., Endoh, T., Yamada, T., Tsuboki, K., Tachibana, Y. and Wakahama, G.,  
595 1990: Determination of a Z-R relationship for snowfall using a radar and high sensitivity  
596 snow gauges, *J. Appl. Meteor.*, **29**, pp. 147–152.

597

598 Garrett, T. J., Fallgatter, C., Shkurko, K. and Howlett, D., 2012: Fallspeed measurement  
599 and high-resolution multi-angle photography of hydrometeors in freefall., *Atmos. Meas.  
600 Tech. Discuss.*, **5**, pp. 4827–4850.

601

602 Hanesch, M., 1999: Fall Velocity and Shape of Snowflake., Ph. D dissertation, Swiss  
603 Federal Institute of Technology., [Available online at  
604 <http://www.distrometer.at/newReferences.html>]

605

606 Heymsfield, A. J., Bansemer, A., Schmitt, C., Twohy, C. and Poellot, M. R., 2004:  
607 Effective Ice Particle Densities Derived from Aircraft Data. *J. Atmos. Sci.*, **61**, pp. 982–  
608 1003.

609

610 Heymsfield, A. J. and Westbrook, C. D., 2010: Advances in the Estimation of Ice  
611 Particle Fall Speeds Using Laboratory and Field Measurements., *J. Atmos. Sci.*, **67**, pp.  
612 2469–2482.

613

614 Hirsikko, A., O'Connor, E., Komppula, M., Korhonen, K., Pfuller, A., Giannakaki, E.,  
615 Wood, C. R., Bauer-Pfundstein, M., Poikonen, A., Karppinen, T., Lonka, H., Kurri, H.,  
616 Heinonen, J., Moisseev, D., Asmi, E., Aaltonen, V., Nordbo, A., Rodriguez, E.,  
617 Lihavainen, H., Laaksonen, A., Lehtinen, K., Laurila, T., Petaja, T., Kulmala, M. and  
618 Viisanen, Y., 2013: Observing Wind, Aerosol Particles, Cloud and Precipitation:  
619 Finland's New Ground-based Remote-sensing Network. *Atmospheric Measurement  
Techniques Discussions*, **6**, pp. 7251-7313.

621

622 Hogan, R. J., Tian, L., Brown, P. R. A., Westbrook, C. D., Heymsfield, A. J. and J.  
623 Eastment, J. D., 2012: Radar Scattering from Ice Aggregates Using the Horizontally  
624 Aligned Oblate Spheroid Approximation. *J. Appl. Meteor. Climatol.*, **51**, pp. 655–671.

625

626 Holroyd, E. W., III, 1971: The meso- and microscale structure of Great Lakes  
627 snowstorm bands: A synthesis of ground measurements, radar data, and satellite  
628 observations. Ph.D. dissertation, *University at Albany, State University of New York*,  
629 p148.

630

631 Huang, G., Bringi, V. N., Cifelli, R., Hudak, D. and Petersen, W. A., 2010: A  
632 Methodology to Derive Radar Reflectivity–Liquid Equivalent Snow Rate Relations Using  
633 C-Band Radar and a 2D Video Disdrometer., *J. Atmos. Oceanic Technol.*, **27**, pp. 637-  
634 651.

635

636 Huang, G., Bringi, V. N., Petersen, W. A., Carey, L., Schultz, C. J. and Gatlin, P. N.,  
637 2011: Case Studies of Winter Precipitation Events Using 2D-Video Disdrometers and C-  
638 Band Radar., *35rd Conf. on Radar Meteorology*, Pittsburgh, PA., Amer. Meteorol. Soc.,  
639 September 26-30., P13.203. [Available online at  
640 <https://ams.confex.com/ams/35Radar/webprogram/Paper191883.html>]

641  
642 Koskinen, J., Poutiainen, J., Schultz, D., Joffre, S., Koistinen, J., Saltikoff, E., Gregow,  
643 E., Turtiainen, H., Dabberdt, W., Pohjola, H., Ruotsalainen, R., Kuitunen, T., Järvi, L.,  
644 Vesala, T., Karppinen, A., Moisseev, D., Göke, S., Pylkkö, P., Hyvärinen, O., Kotro, J.,  
645 Damski, J., Nurmi, P., Kukkonen, J., Viisanen, Y. and Kulmala, M., 2011: The Helsinki  
646 Testbed: A mesoscale measurement, research and service platform. *Bull. Amer.*  
647 *Meteor. Soc.*, **93 (3)**, pp. 325-342.

648  
649 Kruger, A. and Krajewski, W. F., 2002: Two-dimensional video disdrometer: A  
650 description, *J. Atmos. Oceanic Technol.*, **19**, pp. 602-617.

651  
652 Lanza, L., M. Leroy, C. Alexandropoulos, L. Stagi and W. Wauben, 2006: WMO  
653 laboratory intercomparison of rainfall intensity gauges. Instruments and Observing  
654 Methods Report No. 84, WMO/TD-No. 1304, WMO Geneva.

655  
656 Lee, G. and Zawadzki, I., 2005: variability of Drop Size Distributions: Noise and Noise  
657 Filtering in Disdrometric data., *J. Appl. Meteor.*, **44**, pp. 634–652.

658

659 Lim, S., Moisseev, D., Chandrasekar, V. and Lee, D.-R., 2013: Classification and  
660 Quantification of Snow Based on Spatial Variability of Radar Reflectivity. *J. Meteo. Soc.*  
661 *Japan.*, **91**, pp. 763-774.

662

663 Mason, B. J., 2010: The Physics of Clouds., *Oxford University Press*.

664

665 Matrosov, S. Y., Campbell,C., Kingsmill, D. and Sukovich, E., 2009: Assessing Snowfall  
666 Rates from X-Band Radar Reflectivity Measurements. *J. Atmos. Oceanic Technol.*, **26**,  
667 pp. 2324–2339.

668

669 Maxwell-Garnet, J.C., 1904: Colors in Metal Glasses and in Metallic Films., *Phil. Trans.*  
670 *Roy. Soc.*, **A203**, pp. 385-420.

671

672 Mitchell, D. L., 1996: Use of Mass- and Area-dimensional Power Laws for Determining  
673 Precipitation Particle Terminal Velocities, *J. Atmos. Sci.*, **53**, pp. 1710–1723.

674

675 Newman, A. J., Kucera, P. A. and Bliven, L. F., 2009: Presenting the Snowflake Video  
676 Imager (SVI), *J. Atmos. Ocean. Technol.*, **26**, pp. 167–179, 2009.

677

678 Petersen, W. A., L'Ecuyer, T. and Moisseev, D., 2011: The NASA CloudSat/GPM Light  
679 Precipitation Validation Experiment (LPVEx), *The Earth Observer*, **23**, Issue 4.

680

681 Pruppacher, H. R. and Klett, J. D., 2010: Microphysics of Clouds and Precipitation.  
682 (Second revised and expanded edition), Series: *Atmospheric and Oceanographic*  
683 *Sciences Library*, **18**, Springer.

684 Rasmussen R. and 14 co-authors, 2012: How Well are We Measuring Snow, *Bull.*  
685 *Amer. Met. Soc.*, **93**, pp 811-829.

686 Ryzhkov, A. V., Zrnić, D. S. and Gordon, B. A., 1998: Polarimetric Method for Ice Water  
687 Content Determination. *J. Appl. Meteor.*, **37**, pp. 125–134.

688

689 Saltikoff, E., Huuskonen, A., Hohti, H., Koistinen, J. and Järvinen, H., 2010: Quality  
690 Assurance in the FMI Doppler Weather Radar Network., *Boreal Environ. Res.*, **15**, pp.  
691 579–594

692

693 Saltikoff, E., and Nevvonen, L. 2011: First Experiences of the Operational Use of A  
694 Dual-polarisation Weather Radar in Finland., *Meteor. Zeitschrift*, **20**, pp. 323-333.

695

696 Schmitt, C. G. and Heymsfield, A. J. 2010: The Dimensional Characteristics of Ice  
697 Crystal Aggregates from Fractal Geometry., *J. Atmos. Sci.*, **67**, pp. 1605-1616.

698

699 Schönhuber, M., Urban, H. E., Randeu, W. L. and Poiares Baptista, J. P. V., 2000:  
700 Empirical Relationships between Shape, Water Content and Fall Velocity of

701 Snowflakes, *ESA SP-444 Proceedings*, Millennium Conference on Antennas &  
702 Propagation, April 9-14, 2000, Davos, Switzerland.

703

704 Schönhuber, M., Lammer, G. and Randeu, W. L., 2008: The 2D-video-distrometer,  
705 Chapter 1 in *Precipitation: Advances in Measurement, Estimation and Prediction*.  
706 Michaelides, Silas. (Ed.), Springer, ISBN: 978-3-540-77654-3.

707

708 Sekhon R. S., and Srivastava, R. C., 1970: Snow size spectra and radar reflectivity. *J.*  
709 *Atmos. Sci.*, **27**, pp. 299–307.

710

711 Sheppard, B. E. and Joe, P. I., 2008: Performance of the Precipitation Occurrence  
712 Sensor System as a Precipitation Gauge., *J. Atmos. Oceanic Technol.*, **25**, pp. 196-212.

713

714 Szyrmer, W. and Zawadzki, I., 2010: Snow Studies. Part II: Average Relationship  
715 between Mass of Snowflakes and Their Terminal Fall Velocity. *J. Atmos. Sci.*, **67**, pp.  
716 3319–3335.

717

718 Thériault, J. M., Rasmussen, R., Ikeda, K. and Landolt, S., 2012: Dependence of snow  
719 gauge collection efficiency on snowflake characteristics, *J. Appl. Meteor. Climatol.*, **51**,  
720 pp. 745-762.

721

722 Waterman, P. C., 1971: Symmetry, Unitarity, and Geometry in Electromagnetic  
723 Scattering., *Phys. Rev.*, **D 3**, pp. 825-839.

724

725 Wood, N. B., L'Ecuyer, T. S., Bliven, F. L. and Stephens, G. L., 2013: Characterization  
726 of video disdrometer uncertainties and impacts on estimates of snowfall rate and radar  
727 reflectivity. *Atmos. Meas. Tech.*, **6**, pp. 3635-3648.

728

729 Zawadzki, I., Jung, E. and Lee, G., 2010: Snow Studies. Part I: A Study of Natural  
730 Variability of Snow Terminal Velocity., *J. Atmos. Sci.*, **67**, pp. 1591-1604.

731

732 Zhang, G., Luchs, S., Ryzhkov, A., Xue, M., Ryzhkova, L. and Cao, Q., 2011: Winter  
733 Precipitation Microphysics Characterized by Polarimetric Radar and Video Disdrometer  
734 Observations in Central Oklahoma. *J. Appl. Meteor. Climatol.*, **50**, pp. 1558–1570.

735

736

737

738

739

740 **List of Figures**

741 Fig 1: Front- and side-view images of a snow flake from the 2DVD. The maximum ‘size’  
742 is approximately 16 mm in the side view (Camera B); from Huang et al. (2010).

743

744 Fig. 2: Illustrating the measurement principle of the 2D-Video disdrometer (from Kruger  
745 and Krajewski 2002; Schönhuber et al. 2008). Note that the virtual measuring area is  
746 different ( $100 \text{ cm}^2$ ) relative to the single camera measuring area ( $250 \text{ cm}^2$ ).

747

748 Fig. 3: An example to show the shadow area ( $A_e$ ) and the smallest circumscribed area  
749 area ( $A$ ); from Böhm (1989).

750

751 FIG. 4: The map shows the location of 3 C-Band radars (KUM, VAN and KER), the  
752 Järvenpää site and other 6 FMI gauges used in this paper. Note that the OTT-PLUVIO  
753 gauge and 2DVD are sited at Jävenpää.

754

755 FIG. 5: Example of 2DVD-derived fall speeds versus apparent diameter for snow event  
756 from 30 Dec 2010 dominated by snow aggregates. For each size bin the mean and  $\pm 1\sigma$   
757 standard deviation of the fall speed are shown. The exponential fit to the mean values of  
758 the form  $V_f = 1.12 - 1.31 \cdot \exp(-1.42 D_{app})$  where  $D_{app}$  is in mm and  $V_f$  in  $\text{m s}^{-1}$  is also  
759 shown.

760

761 Fig. 6: Particle (snow) size distributions from the 2DVD and from the snow video imager  
762 (SVI) for **(a)** 30 Dec 2010 first snow event with  $\gamma$  equal to 2.21 **(b)** 6 Jan. 2011 event  
763 with  $\gamma$  equal to 2.55.

764

765 Fig. 7: Frequency of occurrence (in color log scale) of  $A_r$  vs.  $D_{app}$  for 30 Dec 2010 snow  
766 event; also shown are the bin averaged mean and  $\pm 1\sigma$  standard deviation bars along  
767 with the power law  $A_r - D_{app}$  fit.

768

769 Fig. 8: Density versus  $D_{app}$  (mean and  $\pm 1\sigma$ ) along with mean  $\rho - D_{app}$  power law fit for the  
770 30 Dec 2010 event.

771

772 Fig. 9: Liquid equivalent snow accumulation for 30 Dec 2010 comparing 2DVD-derived  
773 accumulations against collocated OTT-PLUVIO2 gauge.

774

775 Fig. 10: Time series comparison of reflectivity from 2DVD, POSS and scanning  
776 Kumpula radar for **(a)** 30 Dec 2010 event and **(b)** 6 Jan. 2011.

777

778 Fig. 11: Scatter plot of 2DVD or POSS reflectivity (Y-axis) versus Kumpula radar  
779 reflectivity (X-axis) extracted over Järvenpää site for 30 Dec 2010 event.

780

781 Fig. 12:  $Z_e$  versus SR scatterplot using SIFT method for (a) 30 Dec 2010 case and (b) 6  
782 Jan. 2011. The power law fit using weighted total least squares is also shown.

783

784 Fig. 13: Snow accumulation map for 30 Dec 2010 (entire day) using  $Z_e$ -SR power law in  
785 Table 3. Reflectivity data from three radars have been composited. The solid black dots  
786 are locations of 6 FMI snow gauges and the numbers adjacent are the snow gauge  
787 measurements of liquid equivalent snow accumulation in mm.

788

789 Fig. 14: As in Fig. 13 except the FMI climatological  $Z_e=100*SR^2$  is used.

790

791 Fig. 15: Comparison of hourly accumulations at the Porvoo Harabacka site using FMI  
792 gauge.

793

794 Fig. 16: Scatter plots of daily gauge accumulations from the seven FMI snow gauges  
795 versus radar-based daily accumulations using (top panel **a**) daily  $Z_e$ -SR relations from  
796 Table 3 and (bottom panel **b**) using fixed FMI climatological  $Z_e$ -SR relation. Data from  
797 the 4 snow days are color-coded.

798

799 Fig. 17: Example of SVI images of large aggregates at 1120 UTC on 30 Dec 2010 at  
800 Järvenpää site (also close to time of peak reflectivity, see Fig. 10a).

801

802 Fig. 18: Example of SVI images of large rimed aggregates at 0620 UTC on 06 Jan 2011  
803 at Järvenpää site.

804

805 Fig. 19: Spatial variability of reflectivity (left panel) for 30 Dec 2010 and, (right panel) for  
806 06 Jan cases.

807

808 Fig. 20: RHI scan data from Kumpula radar along the radial to the Järvenpää site (top  
809 panel) 30 Dec 2010 at 1053 UTC, and (bottom panel) 06 Jan 2011 at 0603 UTC.

810

811 Fig. 21: As in Fig. 13 except for 06 Jan 2011 event (0000-0900 UTC only) using 2DVD-  
812 derived  $Z_e$ -SR relation.

813

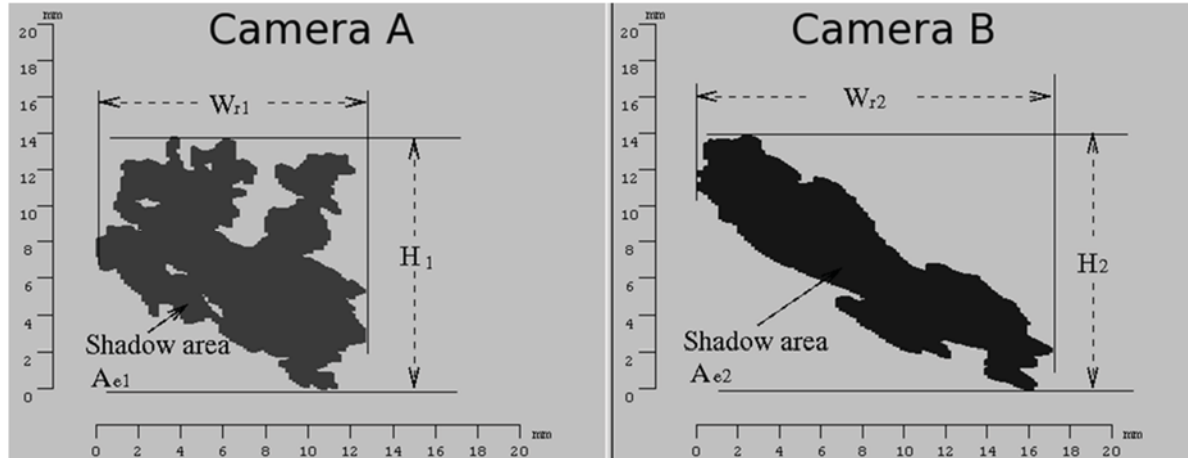


Fig. 1: Front- and side-view images of a snowflake from the 2DVD. The maximum 'size' is approximately 16 mm in the side view (Camera B); from Huang et al. (2010).

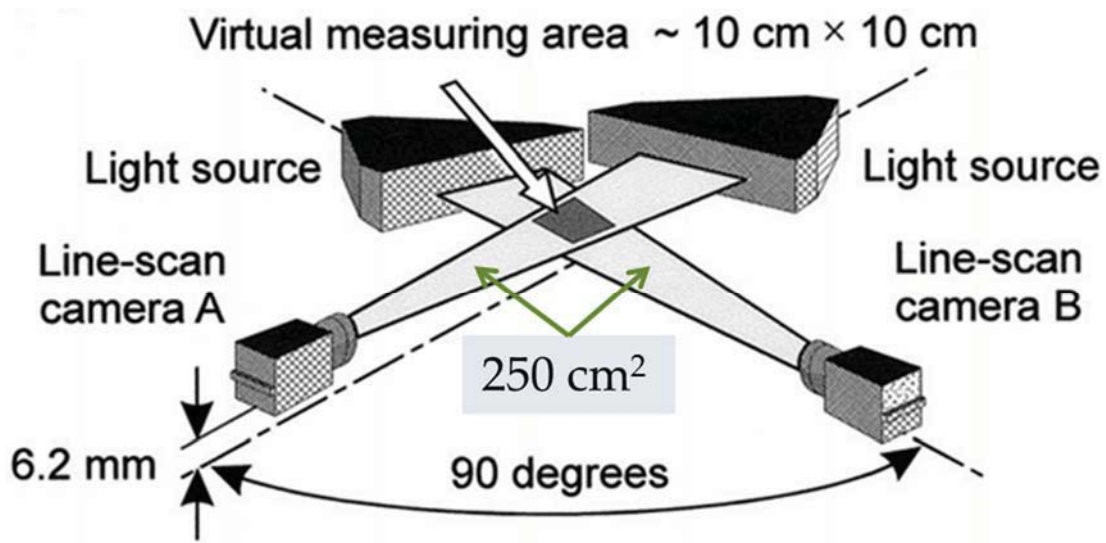


Fig. 2: Illustrating the measurement principle of the 2D-Video disdrometer (from Kruger and Krajewski 2002; Schönhuber et al. 2008). Note that the virtual measuring area is different ( $100 \text{ cm}^2$ ) relative to the single camera measuring area ( $250 \text{ cm}^2$ ).

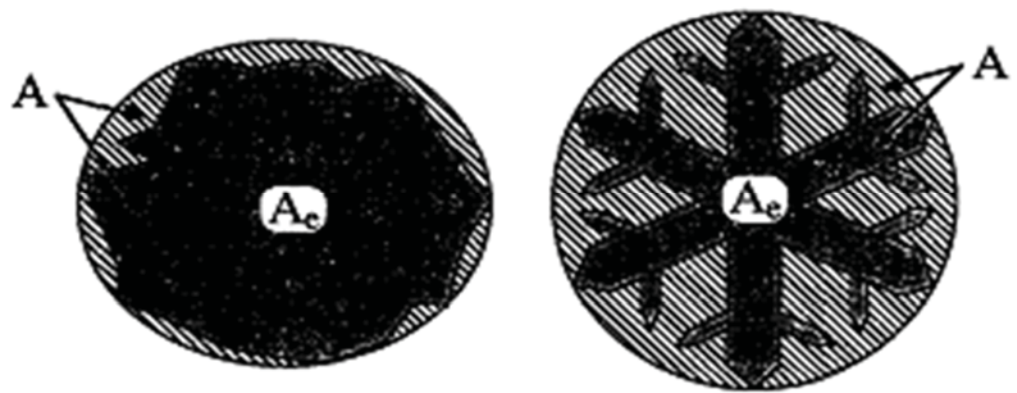
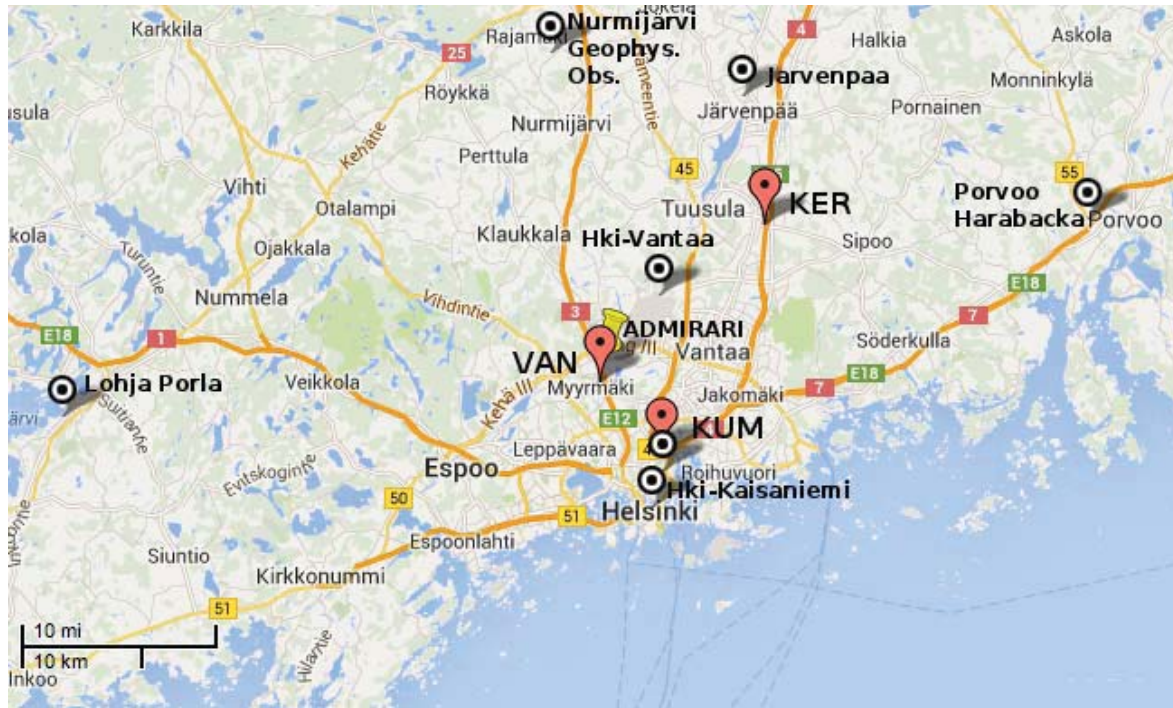
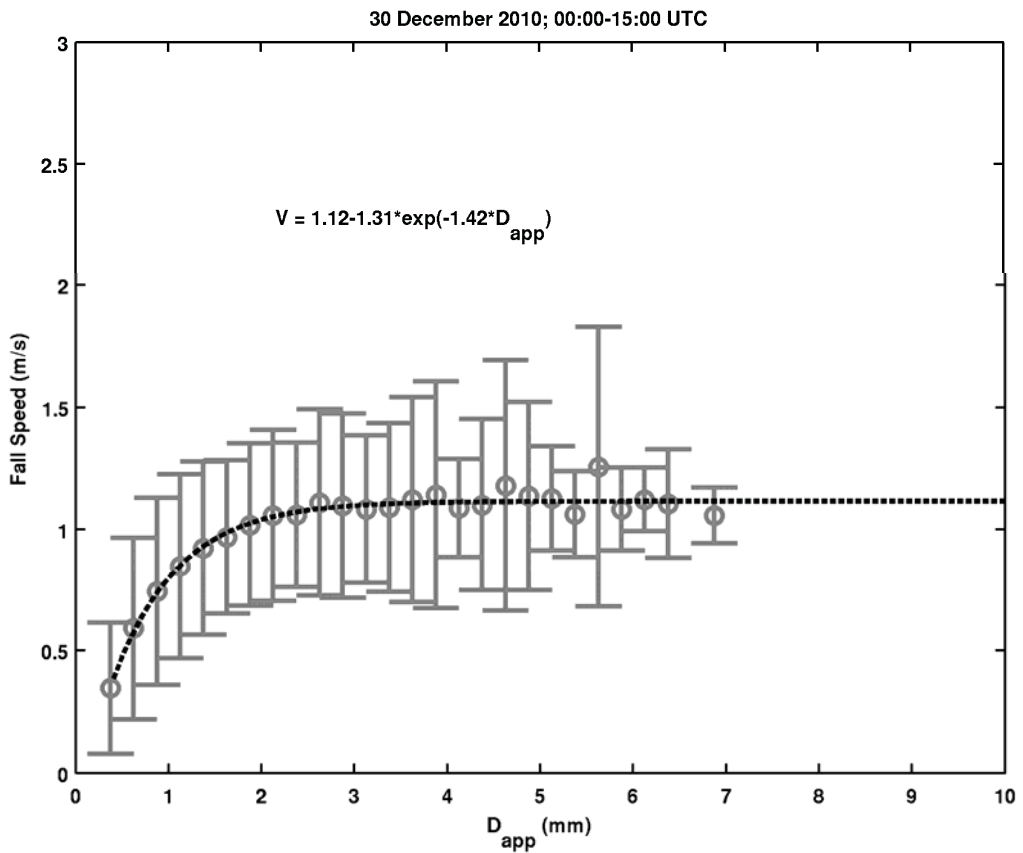


Fig. 3: An example to show the shadow area ( $A_e$ ) and the smallest circumscribed area area ( $A$ ); from Böhm (1989).

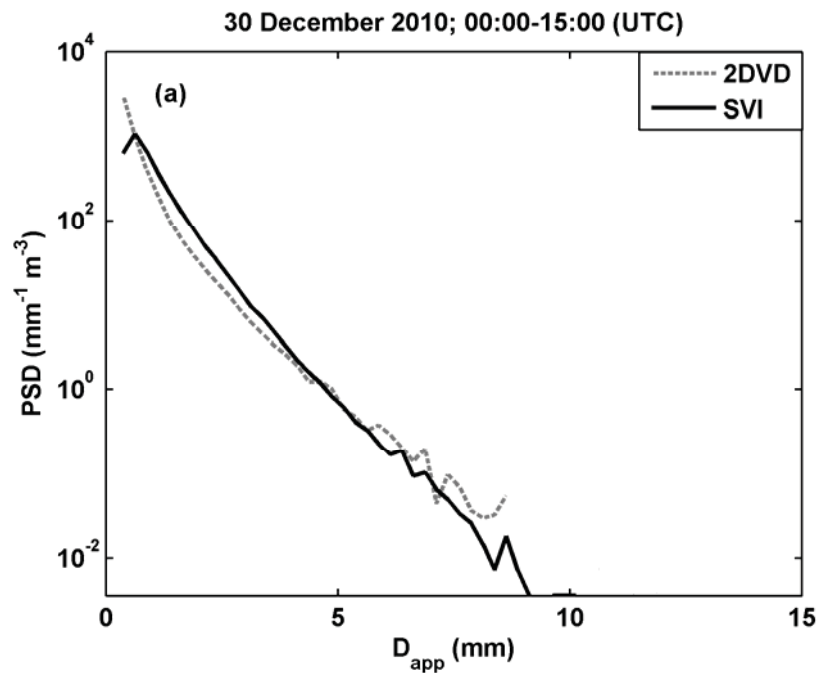


*Fig. 4: The map shows the location of 3 C-Band radars (KUM, VAN and KER), the Järvenpää site and other 6 FMI gauges used in this paper. Note that the OTT-PLUVIO gauge and 2DVD are sited at Jävenpää.*



*Fig. 5: Example of 2DVD-derived fall speeds versus apparent diameter for snow event from 30 Dec 2010 dominated by snow aggregates (00:00-15:00 UTC). For each size bin the mean and  $\pm 1\sigma$  standard deviation of the fall speed are shown. The exponential fit to the mean values of the form  $V_f = 1.12 - 1.31 \exp(-1.42 D_{app})$  where  $D_{app}$  is in mm and  $V_f$  in  $m s^{-1}$  is also shown.*

820



821

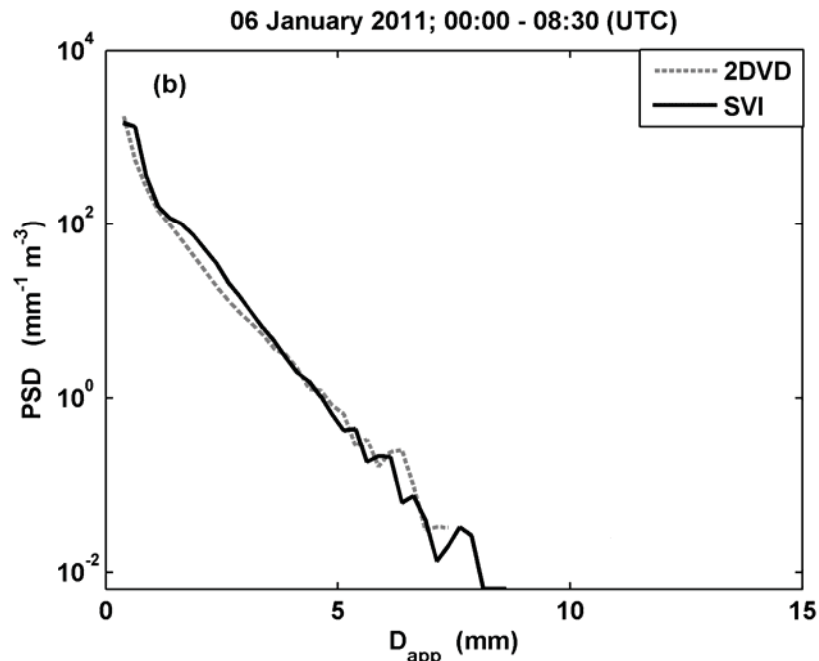
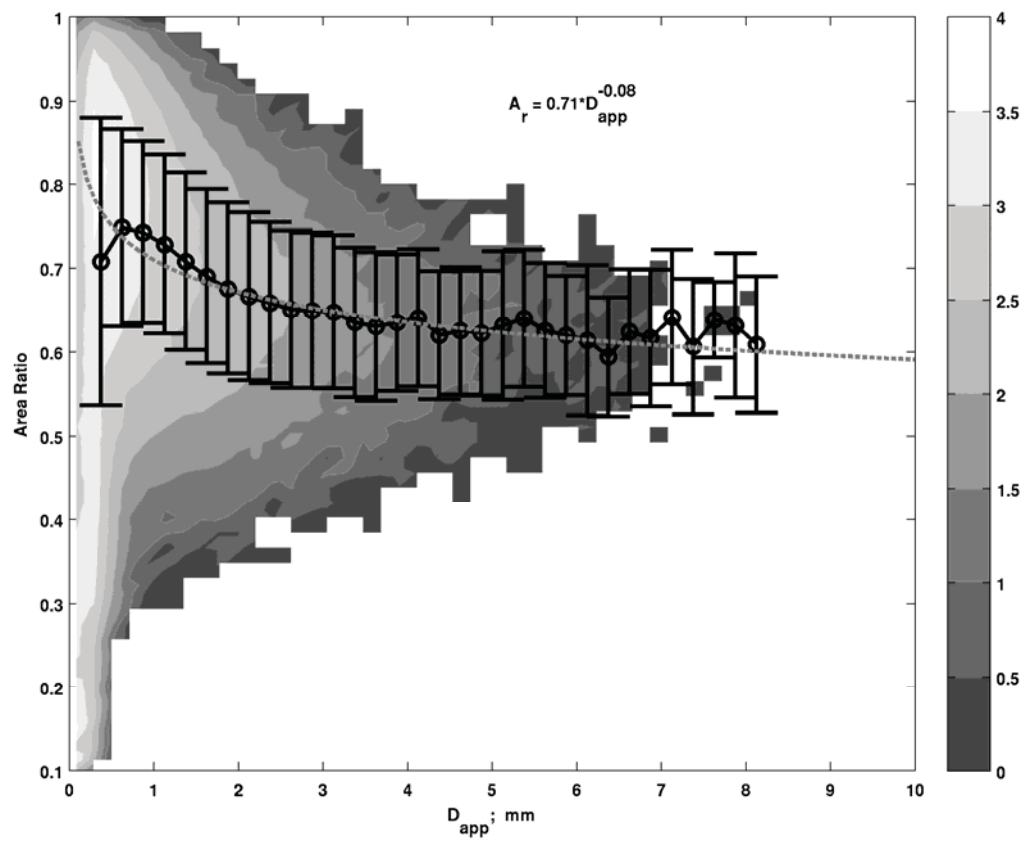


Fig. 6: Particle (snow) size distributions from the 2DVD and from the snow video imager (SVI) for (a) 30 Dec 2010 first snow event with  $\gamma$  equal to 2.21 (b) 6 Jan. 2011 event with  $\gamma$  equal to 2.55.

822



*Fig. 7: Frequency of occurrence (in log scale) of  $A_r$  vs.  $D_{app}$  for 30 Dec 2010 snow event; also shown are the bin averaged mean and  $\pm 1\sigma$  standard deviation bars along with the power law  $A_r - D_{app}$  fit.*

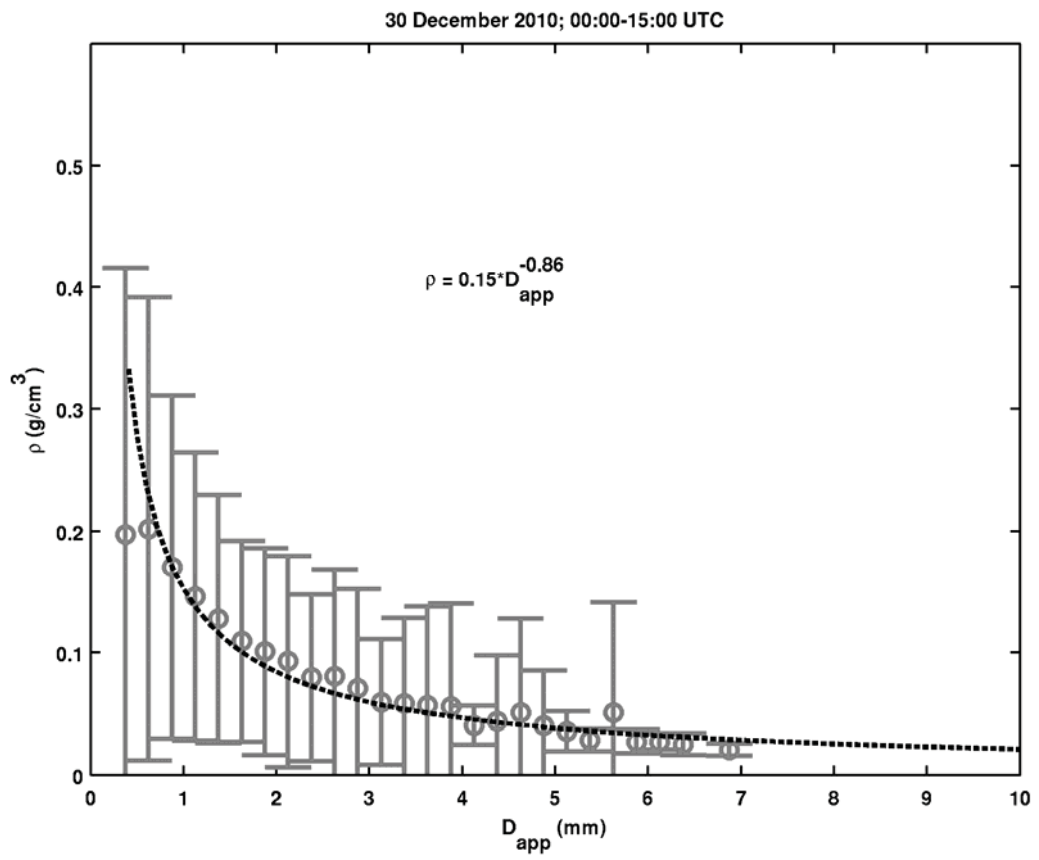


Fig. 8: Density versus  $D_{app}$  (mean and  $\pm 1\sigma$ ) along with mean  $\rho$ - $D_{app}$  power law fit for the 30 Dec 2010 event.

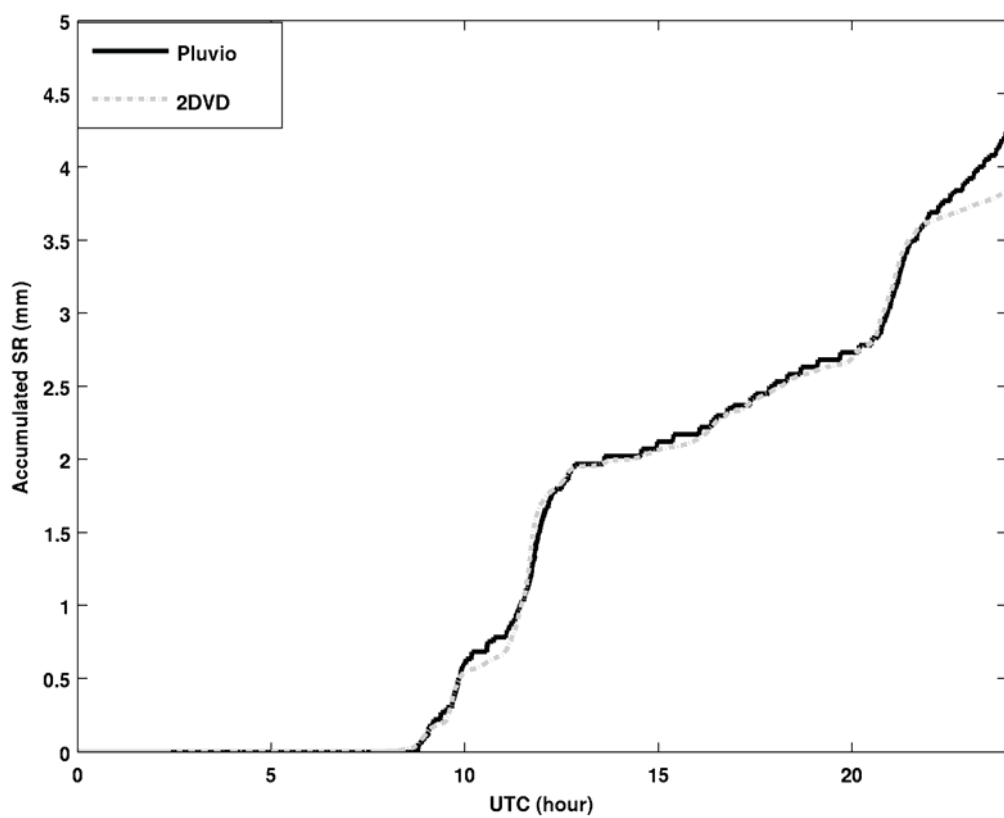
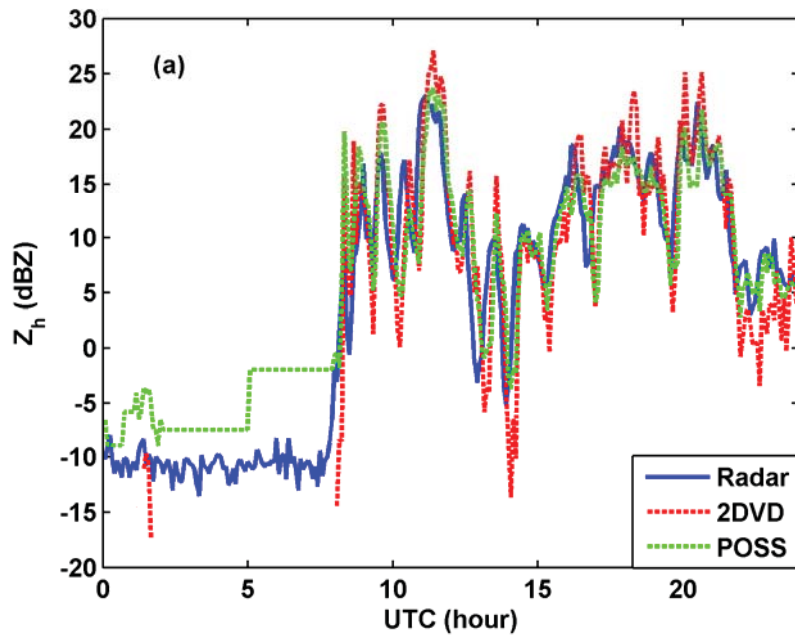
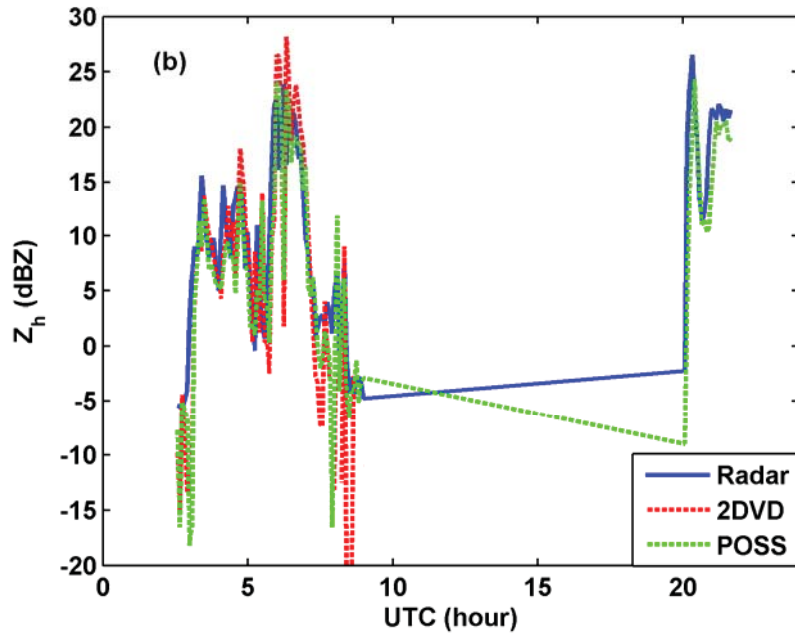


Fig. 9: Liquid equivalent snow accumulation for 30 Dec 2010 comparing 2DVD-derived accumulations against collocated OTT-PLUVIO2 gauge.



826



827

*Fig. 10: Time series comparison of reflectivity from 2DVD, POSS and scanning Kumpula radar for (a) 30 Dec 2010 event and (b) 6 Jan. 2011.*

828

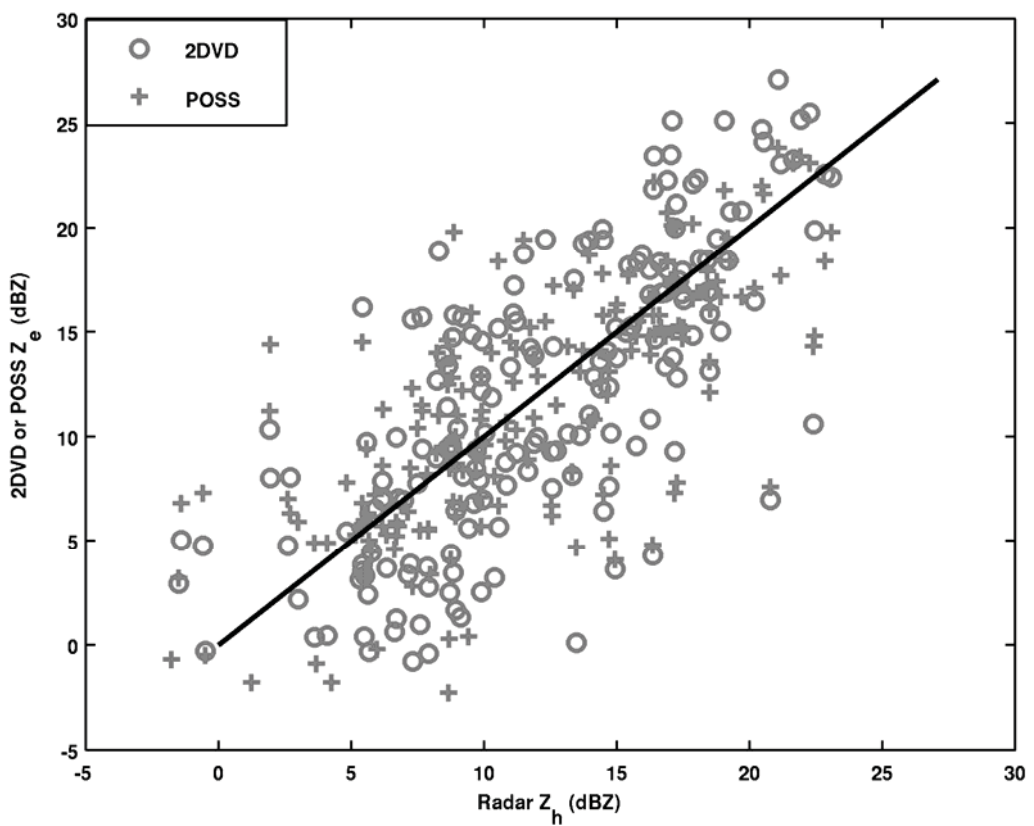


*Fig. 11: Scatter plot of 2DVD or POSS reflectivity (Y-axis) versus Kumpula radar reflectivity (X-axis) extracted over Järvenpää site for 30 Dec 2010 event.*

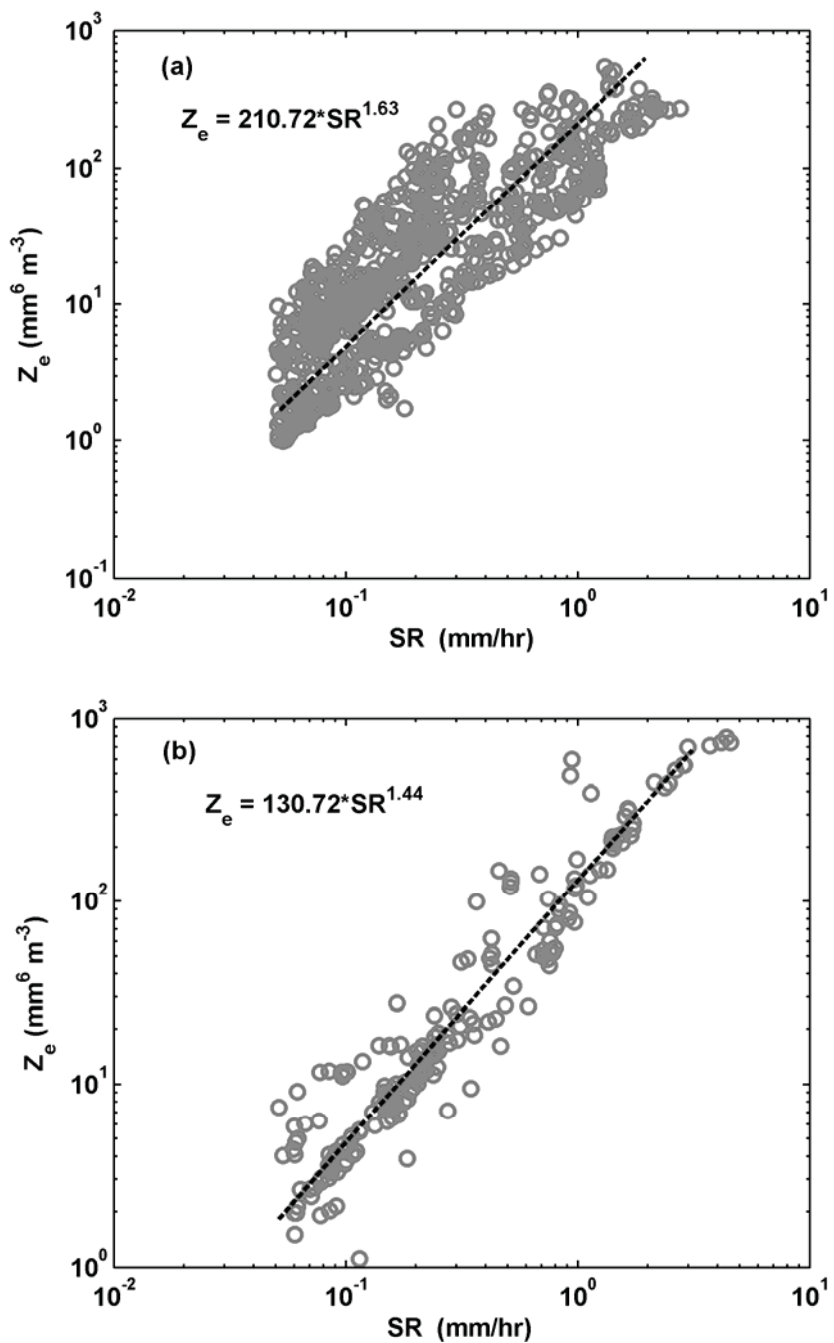


Fig. 12:  $Z_e$  versus  $SR$  scatterplot using SIFT method for (a) 30 Dec 2010 case and (b) 6 Jan. 2011. The power law fit using weighted total least squares is also shown.

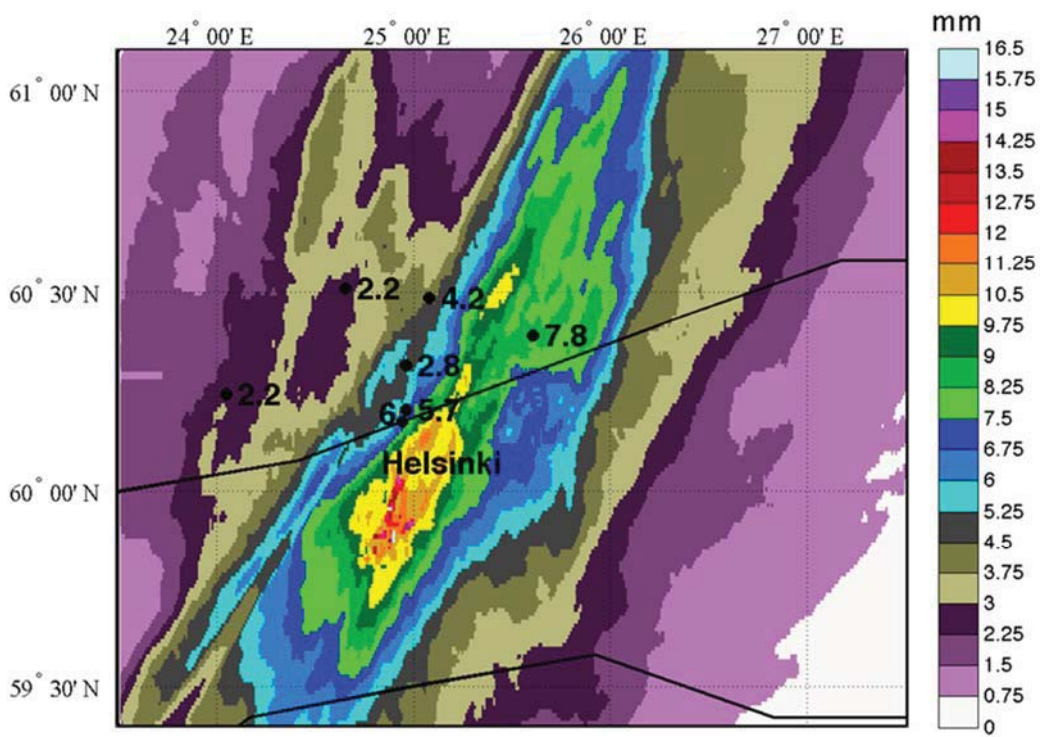


Fig. 13: Snow accumulation map for 30 Dec 2010 (entire day) using  $Z_e$ -SR power law in Table 3. Reflectivity data from three radars have been composited. The solid black dots are locations of 6 FMI snow gauges and the numbers adjacent are the snow gauge measurements of liquid equivalent snow accumulation in mm.

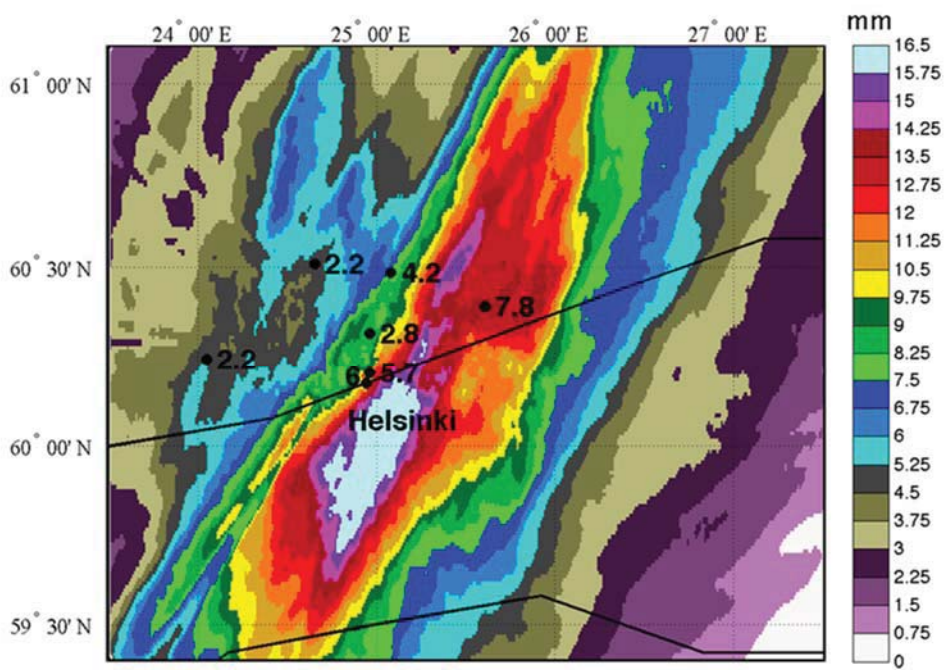


FIG. 14: As in Fig. 13 except the FMI climatological  $Z_e=100*SR^2$  is used.

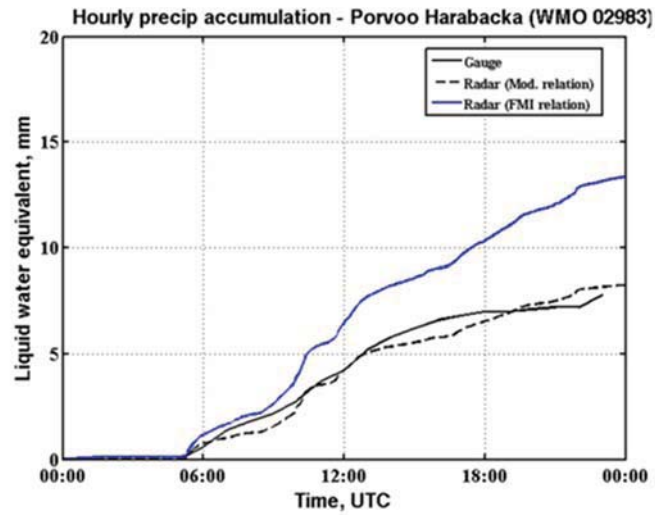


Fig. 15: Comparison of hourly accumulations at the Porvoo Harabacka site using FMI gauge.

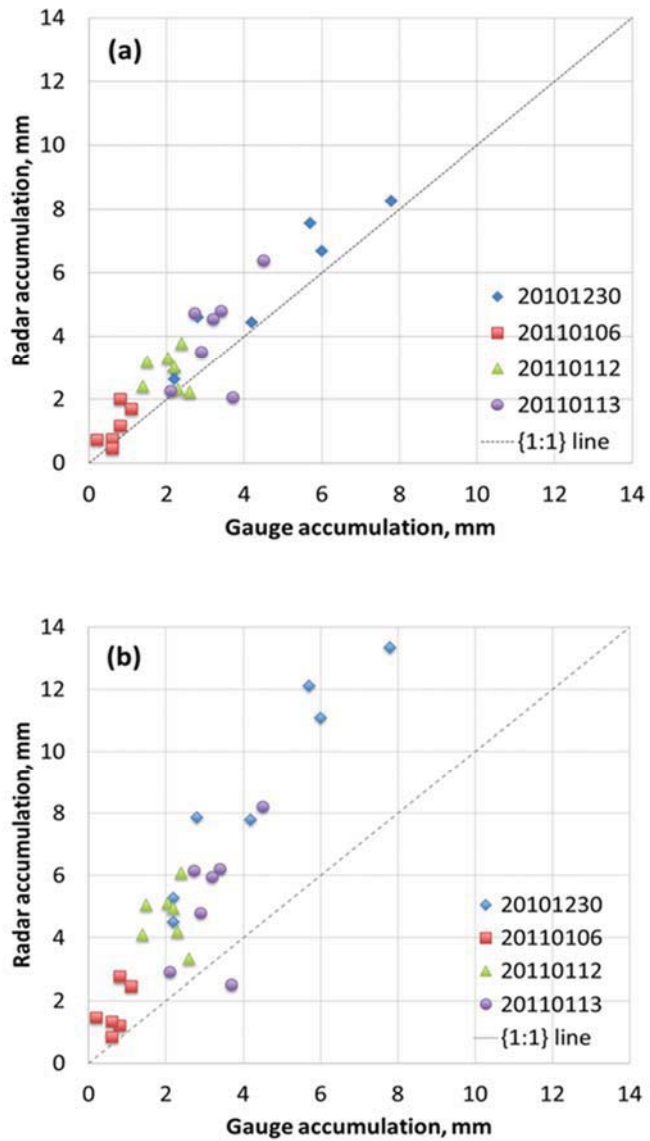


Fig. 16: Scatter plots of daily gauge accumulations from the seven FMI snow gauges versus radar-based daily accumulations using (top panel **a**) daily  $Z_e$ -SR relations from Table 3 and (bottom panel **b**) using fixed FMI climatological  $Z_e$ -SR relation. Data from the 4 snow days are color-coded.

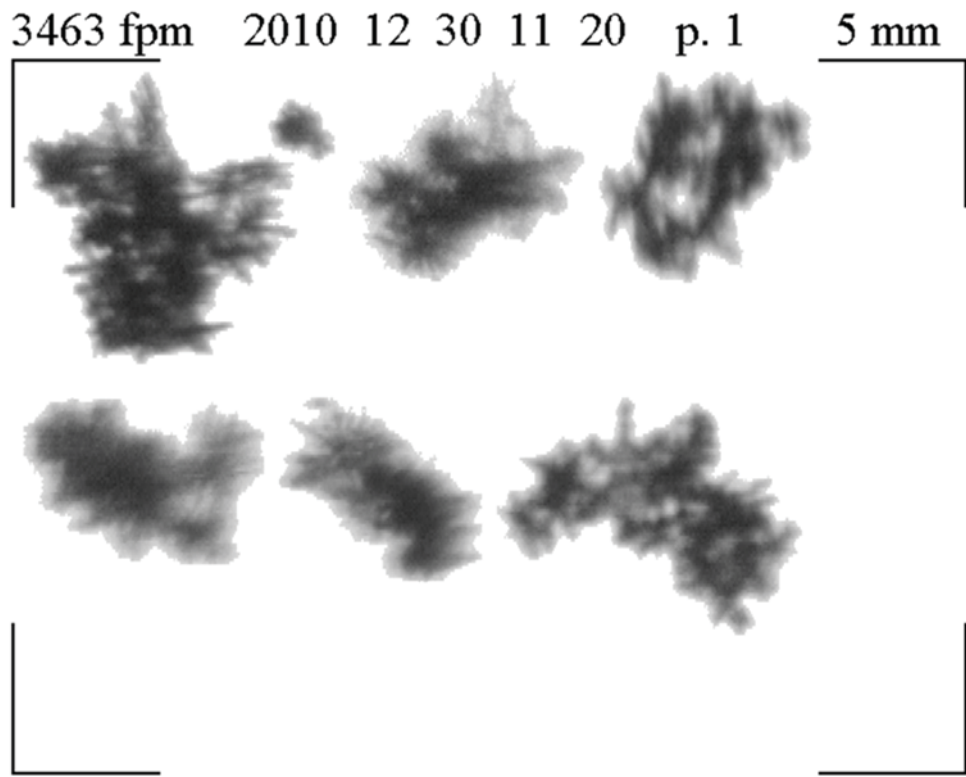
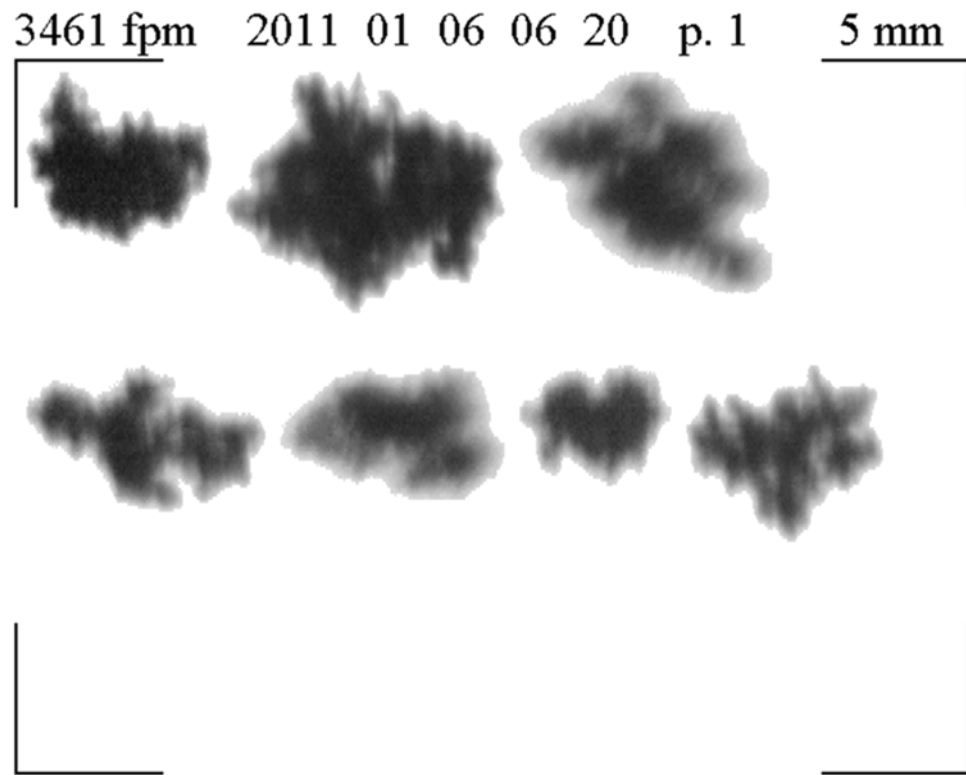
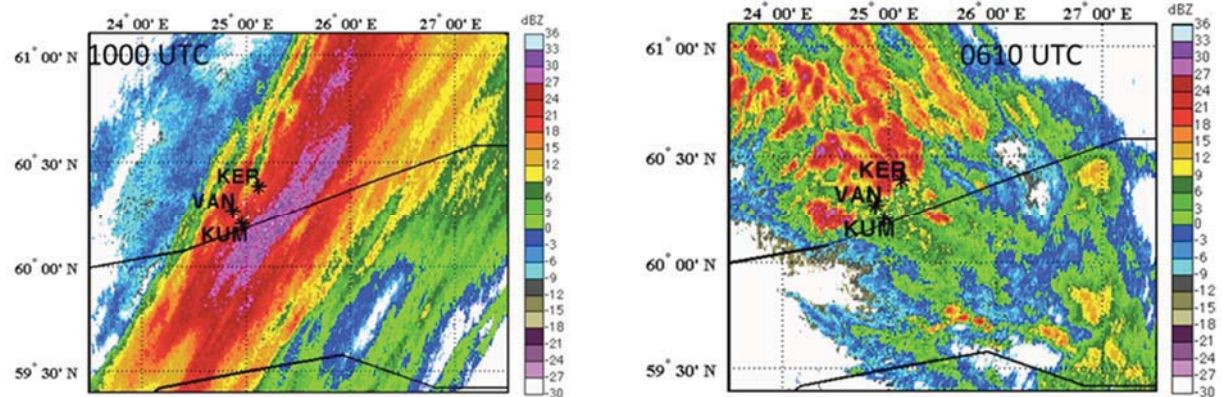


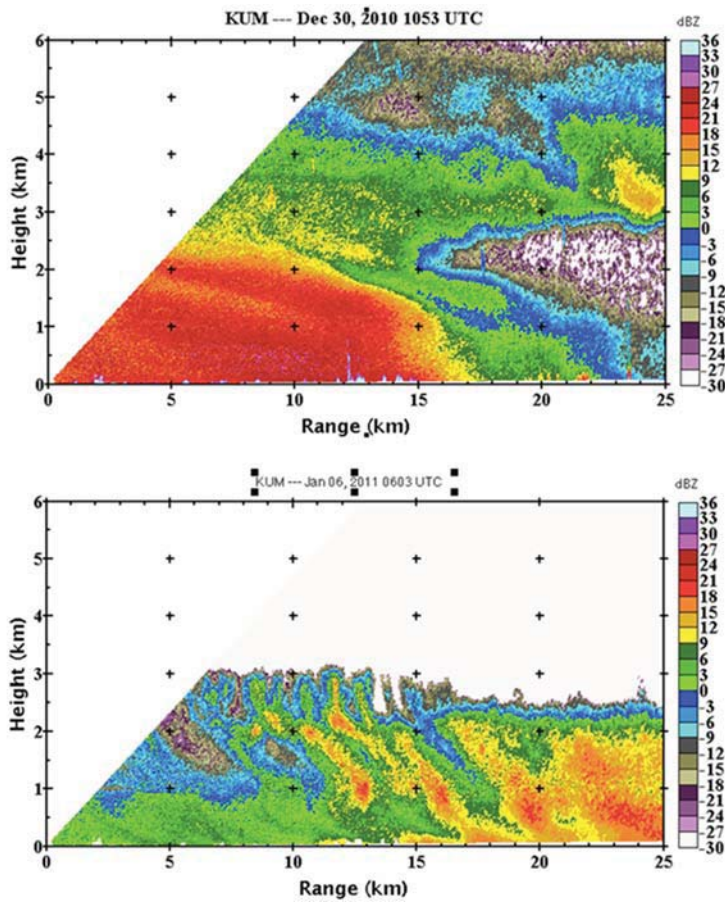
Fig. 17: Example of SVI images of large aggregates at 1120 UTC on 30 Dec 2010 at Järvenpää site (also close to time of peak reflectivity, see Fig. 10a).



*Fig. 18: Example of SVI images of large rimed aggregates at 0620 UTC on 06 Jan 2011 at Järvenpää site.*



*Fig. 19: Spatial variability of reflectivity (left panel) for 30 Dec 2010 and, (right panel) for 06 Jan cases.*



838

*Fig. 20: RHI scan data from Kumpula radar along the radial to the Järvenpää site (top panel) 30 Dec 2010 at 1053 UTC, and (bottom panel) 06 Jan 2011 at 0603 UTC.*

839

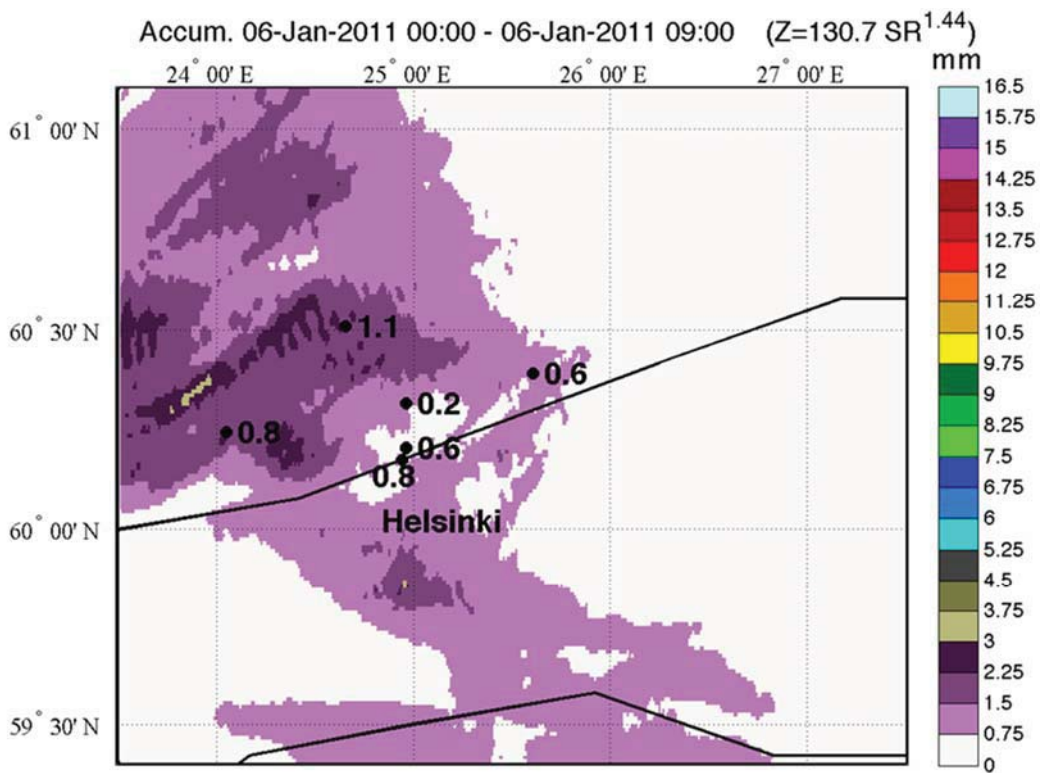


*Fig. 21: As in Fig. 13 except for 06 Jan 2011 event (0000-0900 UTC only) using 2DVD-derived Z<sub>e</sub>-SR relation.*

## LIST of Tables

841 Table 1: The four snow days from LPVEx.

842

843 Table 2: Coefficient  $\alpha$  and exponent ( $\beta$ ) of  $\rho$ - $D_{app}$  power law fit (density in g cm<sup>-3</sup> and  
844  $D_{app}$  in mm)

845

846 Table 3: The  $Z_e = a^*SR^b$  power law for the four days. Note  $Z_e$  in mm<sup>6</sup> m<sup>-3</sup> and  $SR$  in mm  
847 h<sup>-1</sup>.

848

849 Table 4: The  $\gamma$ -adjustment factor and the  $V_f$ - $D_{app}$  fit parameters [ $c$   $d$   $\kappa$ ].

850

851

852 Table 1: The four snow days from LPVEx

Event	Time (UTC)	Temperature C	2DVD accum (mm)	OTT-PLUVIO2 accum (mm)
30 Dec 2010	a.0800-1300 b.1500-2359	a. -9 b. -8	3.84	4.24
06 Jan 2011	0230-0830	-7	1.53	1.53
12 Jan 2011	a.0800-1230 b.2230-2359	a. -3 b. -3	3.36	2.05
13 Jan 2011	0000-0500	-4	2.77	2.73

853

Table 2: Coefficient  $\alpha$  and exponent ( $\beta$ ) of  $\rho$ - $D_{app}$  power law fit (density in g cm<sup>-3</sup> and  $D_{app}$  in mm)

Event	Time (UTC)	$\alpha$	$\beta$
30 Dec 2010	a.0800-1300	a. 0.15	-0.86
	b.1500-2359	b. 0.15	-0.96
06 Jan 2011	0230-0830 <sup>†</sup>	0.17	-0.79
12 Jan 2011	a.0800-1230	a. 0.23	-0.88
	b.2230-2359	b. 0.19	-0.8
13 Jan 2011	0000-0500	0.19	-0.8

† the 2DVD stopped working at 0824 on this day

Table 3: The  $Z_e = a^*SR^b$  power law for the four days. Note  $Z_e$  in  $\text{mm}^6 \text{ m}^{-3}$  and  $SR$  in  $\text{mm h}^{-1}$ .

	a	b
30 Dec. 2010	210.72	1.63
06 Jan. 2011	130.72	1.44
12 Jan. 2011	209.20	1.67
13 Jan. 2011	134.86	1.81

855 † The power laws are derived for application to all events occurring during the  
856 day.  
857

Table 4: The  $\gamma$ -adjustment factor and the  $V_f$ - $D_{app}$  fit parameters [c d  $\kappa$ ].

Event	Time (UTC)	$\gamma$	$\gamma_{SVI}$	c	d	$\kappa$
30 Dec 2010	a.0800-1300	a. 2.21	a. 2.46	1.20	1.54	1.16
	b.1500-2359	b. 1.94	b. 2.57			
06 Jan 2011	0230-0830	2.55	2.92	1.37	1.37	1.25
12 Jan 2011	a.0800-1230	a. 3.53	a. 3.6	1.37	1.85	1.78
	b.2230-2359	b. 2.23	b. 2.18			
13 Jan 2011	0000-0500	2.23	4.24	1.34	1.34	0.95

† The  $V_f$ - $D_{app}$  fits are derived for application to all events occurring during the day (note:  $D_{app}$  in mm and  $V_f$  in  $m s^{-1}$  ).